



Numerical Studies of Spacecraft-Plasma Interaction: Simulations of Wake Effects on the Cluster Electric Field Instrument EFW

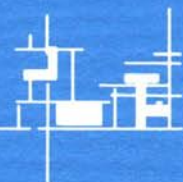
ERIK ENGWALL

IRF Scientific Report 284
February 2004

ISSN 0284-1703

INSTITUTET FÖR RYMDFYSIK
Swedish Institute of Space Physics

Uppsala, Sweden



**Numerical Studies of Spacecraft-Plasma Interaction:
Simulations of Wake Effects on the
Cluster Electric Field Instrument EFW**

ERIK ENGWALL

*Swedish Institute of Space Physics
P.O. Box 537, SE-751 21 Uppsala, Sweden*

IRF Scientific Report 284
February 2004

Printed in Sweden
Swedish Institute of Space Physics
Kiruna 2004
ISSN 0284-1703

Abstract

The Cluster satellites are designed for scientific exploration of fields, waves and particles in our space environment. Since their launch three years ago they have provided valuable information from different regions in space. The interpretation of the data is based on a good understanding of the function of the instruments and how they are affected by the surrounding space plasma. When operating in the polar wind, the Cluster electric field instrument EFW has indicated an apparent electric field, which is caused by interactions between the satellite and the plasma particles. The polar wind consists of a cold tenuous plasma, flowing up from the Earth's magnetic poles along the geomagnetic field lines. In this environment, negatively charged wakes may form behind the Cluster satellites. These wake structures will influence the electric field measurements from EFW, thus creating a false electric field. To get a more profound knowledge about the wake formation and its impact on EFW, we have used the simulation package PicUp3D to carry out numerical simulations of a flowing plasma interacting with a spacecraft. The simulation results provide proof of the existence of a deep wake and also a quantitative estimation of the apparent electric field, which is consistent with satellite data.

Contents

1	Introduction	2
2	Space plasma	3
2.1	The space environment	3
2.2	Properties of a plasma	4
2.3	Spacecraft-plasma interaction	5
3	Electrostatic wake in Cluster data	7
3.1	The Cluster satellites	7
3.2	Electric field measurements from Cluster	7
3.3	Enhanced wake formation behind Cluster	10
4	Numerical simulations with <i>PicUp3D</i>	13
5	Simulations of the Cluster phenomena	19
5.1	Booms only	20
5.2	Spacecraft body without booms	25
5.3	Further simulations	30
5.3.1	Numerical variations	30
5.3.2	Variation of plasma parameters	32
6	Discussion	34
7	Conclusions	36
8	Acknowledgements	38

1 Introduction

The environment in space affects us more than we normally expect. For example, during periods of large solar activity, such as the recent violent solar storm (November 2003), equipment for navigation and communication can be disturbed and in worst case destroyed. The solar wind, which consists of high energy solar particles, is blowing in the whole solar system and will increase in strength when the Sun is in an active phase. The Earth is protected from the solar wind mainly by its magnetic field, creating a shield around the Earth, called the magnetosphere. To get a better understanding of the processes in the magnetosphere, the solar wind and the areas in between, a large number of scientific satellites have been launched during the past 30 years. The Cluster II mission is one of today's most ambitious projects, with four satellites flying in formation to explore some of the key regions in the near-Earth space.

A spacecraft will always interact with the surrounding particles in space. One consequence of these interactions is that the spacecraft can charge to high potentials, which can be of great concern if the charge distribution is uneven, since this will lead to discharges possibly destroying critical systems on the spacecraft. The Cluster satellites, which are always charged to small positive potentials, will not experience such problems due to their conductive surfaces. Even if the satellites are not affected themselves, the measurements from the on-board scientific instruments can be disturbed. This is evident for the electric field measurements from the *Electric Fields and Waves instrument* (EFW), which shows spurious electric fields in the cold and tenuous polar wind. The source of the disturbance has been interpreted as a negatively charged wake forming behind the spacecraft due to the positive spacecraft potential [1]. The objective of this project is to verify this model and quantify the effect on the electric field instrument using numerical simulations.

In the numerical study, we have used the open-source simulation code package *PicUp3D*, which is fully written in JAVA and therefore extremely portable. It has been developed to study different types of interactions between spacecraft and the surrounding particles in space, including wake effects. The main goal of the numerical study is to examine the errors in the electric field instrument. However, we are also interested in the performance of the simulation package and to see to what extent the wake can be modelled. Hence, this report will have both physical and numerical aspects.

Section 2 includes a treatment of the space environment, introducing the notion of *plasmas*, which is the dominant state of matter in the universe, and a description of spacecraft-plasma interactions. In section 3, we examine the Cluster satellites, the electric field instruments and the existence and formation of a wake behind the satellites. PicUp3D is the subject of section 4 and in section 5 the results from the simulations can be found. Sections 6 and 7 contain a discussion and concluding remarks.

2 Space plasma

2.1 The space environment

Space and phenomena in the sky have fascinated mankind for millennia. With the invention of the telescope and its further development, discoveries revealing some of the mysteries of our solar system, galaxy and the whole universe have been made. Nevertheless, it was not until the satellite era, which started with the launch of the Soviet satellite Sputnik 1 in 1957, that it was possible to explore the near-Earth space environment in detail. An adequate description of this environment is necessary to understand such a common and relatively close phenomenon as the aurora borealis. This section is intended to give a brief introduction to the space environment around us. For a more detailed description, books on space physics, for example [2], [3] and [4], are recommended.

The existence of the Sun is necessary, either directly or indirectly, for all life on Earth. As everybody knows, energy is transported from the Sun in form of electromagnetic radiation, which for example will give us enough heat and light and allow plants to grow. What is less known, is that as much as 1% of the energy from the Sun reaching the Earth is in form of charged particles [5]. The Sun does, in fact, not only emit light, but also a high-speed stream of particles, at a rate of 1 million tons/s. This stream is called the *solar wind* consisting of *plasma*, which is an ionized gas. The solar wind plasma originates in the outer layers of the Sun, thus consisting mostly of protons, electrons and a small amount of helium ions. Some of these particles will eventually reach the Earth, but this is only a tiny fraction of all the particles in the solar wind, since the Earth is shielded by its magnetic field. This magnetic shield protects us from the highly energetic solar wind plasma, which has an average speed of 450 km/s and temperature of 100 000 K.

The solar wind is deflected around the Earth's magnetic field, compressing it in the sunward direction and extending it in the anti-sunward direction (see figure 1). Since the solar wind is supersonic at the orbit of the Earth, a shock wave will form around the Earth reducing the speed of the solar wind plasma to subsonic values. This happens at the *bow shock*. Shocked solar wind particles continue into the *magnetosheath*, where they are re-accelerated to supersonic flow velocities. The *magnetopause* is the border to the Earth's *magnetosphere*, which is the region dominated by the Earth's magnetic field. The solar wind experiences difficulties to enter the magnetosphere through the magnetopause. However, in the *cusp* regions the magnetic field lines of the solar wind are connected to the Earth's magnetic field, which will allow solar wind plasma to penetrate the magnetosphere. The *magnetotail* is a cold tenuous region in the magnetosphere, extending from the dusk side of the Earth far out into the solar wind. Also in the *plasma sheet* the plasma density is low, but here the particle energies are high, making the plasma hot. The *plasmasphere* is the torus-shaped region closest to the Earth with a cold dense plasma. Above the geomagnetic poles, the *polar caps* are found. They are bounded by the auroral regions, where the aurora borealis¹ appears, when charged particles (mostly electrons) from the magnetosphere enter the atmosphere of the Earth and collide with atoms and molecules, typically at an altitude of 100 km. In the collisions, the atmospheric atoms and molecules will be excited, and when de-excited, light will be emitted. This light can be seen in the sky at clear nights.

Most of the plasma in the magnetosphere originates from the ionosphere, which is the

¹The aurora borealis is observed on the northern hemisphere, while the same phenomenon on the southern hemisphere is called *aurora australis*.

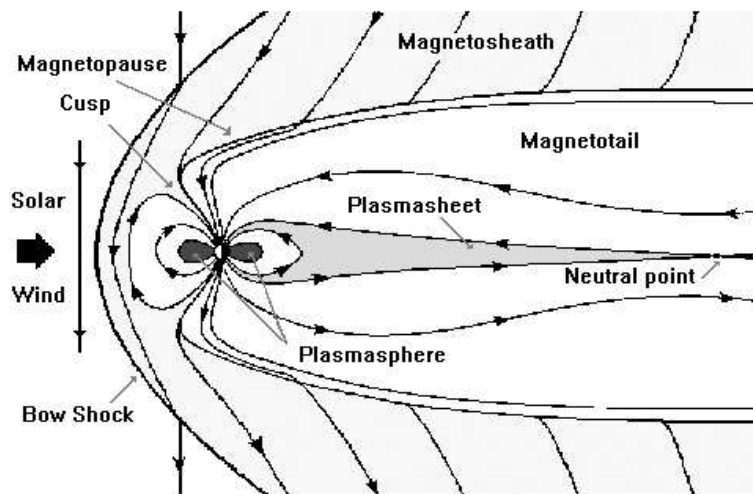


Figure 1: A schematic picture of the Earth's magnetosphere (from <http://www.space-plasma.qmw.ac.uk/>).

upper part of the atmosphere, where the ionization caused by the ultraviolet radiation from the Sun becomes important. If the ionospheric plasma is sufficiently energized, it can escape into the magnetosphere by several different processes. An example of such a process is the *polar wind*, which is an up-flowing stream of ionospheric plasma along the open geomagnetic field lines in the polar cap. In this region, some previously unnoticed wake effects have been discovered in the data from the EFW instrument on the Cluster satellites. Understanding these measurement problems is the rationale for this report, so the polar wind plasma is the environment we will be modelling. In this study we investigate problems at an altitude of around $8 R_E$, where the polar wind is mainly constituted of H^+ (83%), O^+ (14%) and He^+ (3%). At this altitude, the polar wind plasma is cold (1-2 eV for H^+) and tenuous ($\sim 0.3 \text{ cm}^{-3}$ for H^+) [6].

2.2 Properties of a plasma

Plasma is the dominating state of matter in the universe, estimated to comprise around 99% of all observable matter. The lower part of the Earth's atmosphere is one of the few exceptions, where plasma does not play an important role. Because of this abundance of plasma in the universe, we will need knowledge in plasma physics to understand phenomena in space. Even a short comprehensive summary of the theory of plasma physics is beyond the scope of this report². However, we need to know some basic principles for the study of the source of the spurious electric field in the measurements from Cluster.

One important feature of a plasma is that it will exhibit *collective behaviour*, which means that the plasma particles will be governed by the long-range electromagnetic forces instead of collisions like in a normal gas. The phenomenon of *Debye shielding* is a fundamental property of a plasma and gives an example of collective behaviour. When a charged object is immersed in a plasma, the potential around it will be shielded out by either the ions or the electrons. A positively charged object will namely attract a cloud of electrons, while a negatively charged object will be enclosed in an ion cloud. If the plasma is cold, the shielding will be perfect outside the cloud. For warmer plasmas, however, the small potentials at the edge of the clouds, will not be able to prevent

²[7] gives a good introduction to plasma physics and is used as the main reference for this section.

the electrons or ions from escaping. To get a notion of the size of the shielding cloud, we introduce the *Debye length*, which is a characteristic length for the shielding of the potential around a charged object. The Debye length, λ_D , is defined by the expression

$$\lambda_D = \sqrt{\frac{\epsilon_0 K T_e}{n q_e^2}}, \quad (1)$$

where ϵ_0 is the constant of permittivity, K the Boltzmann constant, T_e the electron temperature, n the plasma density³ at infinity and q_e the electron charge. It is worthwhile to note that the Debye length will increase when the temperature increases, which can be explained by the fact that the augmentation of the thermal motion of the plasma particles will make the shielding weaker. Conversely, a dense plasma will make the Debye length shorter, as there are more particles to shield out the potential. A criterion for a plasma is that it is *quasineutral*. This is fulfilled when the dimensions of the physical system are much larger than the Debye length, since every local concentration of charge will be shielded in a distance much smaller than the size of the system.

Considering only the individual plasma particles, we can find some useful relations for their motion in electromagnetic fields, here taken to be constant both in time and space. The equation of motion for a particle with mass m , charge q and velocity \mathbf{v} under the influence of an electric field \mathbf{E} , and a magnetic field \mathbf{B} is given by

$$m \frac{d\mathbf{v}}{dt} = q(\mathbf{E} + \mathbf{v} \times \mathbf{B}) \quad (2)$$

If the electric field is zero ($\mathbf{E} = \mathbf{0}$) and \mathbf{v} is perpendicular to \mathbf{B} , equation 2 only describes a circular motion with the Lorentz force as the central force ($\mathbf{F}_c = q\mathbf{v} \times \mathbf{B}$). The angular frequency of this motion is the *cyclotron angular frequency*, $\omega_c = \frac{|q\mathbf{B}|}{m}$, and the radius is the *Larmor radius*, $r_L = \frac{v}{\omega_c}$. If the velocity has a component along the magnetic field, the particle will move in a spiral. The projection of the motion onto the plane perpendicular to \mathbf{B} will, however, still be a circle with the same center as before. For non-zero electric fields the particle will drift with a velocity $\mathbf{E} \times \mathbf{B}/B^2$, thus in a direction perpendicular to both the electric and magnetic fields.

Because of the electromagnetic properties of plasma, different types of oscillations will arise. The simplest type are the *plasma oscillations*. The light electrons will, because of their inertia, oscillate back and forth against a uniform background of massive immobile ions, with a characteristic frequency, the *plasma frequency*. The plasma frequency, ω_{pe} is given by

$$\omega_{pe} = \sqrt{\frac{n_0 e^2}{\epsilon_0 m}} \quad (3)$$

The quantity ω_{pe}^{-1} is often chosen as a characteristic time scale for plasmas.

2.3 Spacecraft-plasma interaction

Spacecraft interact with the particles in the surrounding plasma, which has many consequences for both the spacecraft itself and the plasma environment. One of the phenomena of great importance is *spacecraft charging*. This area has been subject to extensive research, especially for commercial satellites, since the potential of a spacecraft

³The plasma density is expressed in particles per unit volume.

in a dense plasma can reach high negative values of the order of kV. If the spacecraft is charged unevenly, hazardous electrostatic discharges between different parts of the spacecraft may occur, which will affect the performance of the satellite. In the Cluster case the problems of spacecraft charging are not that dramatic. Firstly, the Cluster satellites are designed with a conductive surface, which will prevent an uneven charge distribution. Therefore, discharges will never occur, even if the satellites are charged to high potentials. Secondly, the Cluster satellites are charged to positive potentials from a few volts to a few tens of volts positive, since sunlit spacecraft in magnetospheric plasmas will charge positively due to emission of photoelectrons. Spacecraft charging will therefore have no severe impact on the satellite itself. However, if the spacecraft has a relative motion with respect to the plasma the positive potential of the spacecraft will give rise to a negatively charged *wake* behind the satellite, which will affect the electric field measurements. This is what happens for Cluster (see section 3.3).

The process of spacecraft charging can be understood by examining a conductive object immersed in a plasma [8]. Even for non-flowing plasmas, the object will be hit by plasma particles due to their thermal motion. The particles are collected by the object, and at thermal equilibrium it will become negatively charged: Ions and electrons have the same energy at thermal equilibrium, but the electrons move faster, because of their much lower mass. This results in the electrons hitting the object more frequently, leading to a net negative charge. If there are no other charging effects, the potential will finally adjust itself at a value, where the currents of electrons and ions balance each other. For Cluster the emission of photoelectrons is also important and in other cases there exist further charging effects. In any case, the spacecraft will reach equilibrium, when the total current to its surfaces is zero. The general spacecraft charging relation [9] is given by

$$I_e - [I_i + I_{bse} + I_{se} + I_{si} + I_{ph}] + I_b = 0. \quad (4)$$

I_e and I_i are the currents of electrons and ions incident on the spacecraft surface, respectively. The term I_{bse} is the current of backscattered electrons due to I_e . The currents I_{se} and I_{si} consist of secondary electrons, emitted when electrons and ions hit the spacecraft. In the Cluster case the secondary electron emission is negligible compared to the photoelectron current I_{ph} , which is the main cause of the positive spacecraft potential. In tenuous plasmas, like in the polar wind, the photoelectron current will be dominant over all other currents and the spacecraft will reach a positive potential, where most of the photoelectrons are recollected by the spacecraft, and it is only the small fraction of high energy photoelectrons escaping into the ambient plasma that will establish an equilibrium with the other currents [10]. I_b , finally, is the current from a possible active ion source installed on the spacecraft, which is used for example for propulsion or potential control. Cluster is equipped with a potential control device, called ASPOC⁴ [11], and it operates successfully reducing the spacecraft potential to constant values of a few volts. In addition to these currents, there could also be currents between adjacent surfaces, if they are charged to different potentials. In addition to these currents, one may have to consider displacement currents for time-dependent problems.

⁴Active Spacecraft Potential Control.

3 Electrostatic wake in Cluster data

3.1 The Cluster satellites

The Cluster mission consists of four identical scientific spacecraft investigating space- and time-varying phenomena in the Earth's magnetosphere [12]. In 1996 the first four Cluster satellites (Cluster I mission) were launched with one of the Ariane-5 rockets. Unfortunately, this mission met a premature end, when the rocket exploded only 37 seconds after launch. The second trial in the summer of 2000 was more successful and the Cluster II mission has now been fully operational for more than three years, which should be compared to its expected life time of five years. The Cluster mission is regarded as a key mission for the European Space Agency, ESA, and has up to date provided a vast range of revealing data.



Figure 2: An artistic impression of the four Cluster satellites (from <http://sci.esa.int>).

The four satellites are orbiting the Earth in a tetrahedral formation, which allows simultaneous measurements at different locations in the magnetosphere. Each satellite carries 11 instruments for charged particle detection and field and waves measurements. The main goal of the Cluster mission is to investigate phenomena in the following key regions of the magnetosphere: *the solar wind, the bow shock, the magnetopause, the polar cusp, the magnetotail and the auroral zones*. To achieve this goal, the satellites have elliptical polar orbits with perigee at 4 RE and apogee at 19.6 RE⁵, thus passing through all the key regions in a period of 57 h (see figure 3). The satellites are cylindrical with a height of 1.3 m and diameter of 2.9 m. Their launch mass was 1200 kg, of which 650 kg was propellant and 71 kg scientific payload. The satellites are spinning with a period of 4 s.

3.2 Electric field measurements from Cluster

Measurements of electric fields are of great importance in understanding several processes in space plasma physics, such as magnetic reconnection⁶ and particle acceleration [1]. The Cluster satellites are equipped with two instruments for electric field measurements using different techniques: the Electric Fields and Waves instrument (EFW) [13], [14] and the Electron Drift Instrument (EDI) [15], [16]. EFW uses the well-known

⁵The nominal value of the radius of the Earth (RE) is 6371.2 km.

⁶Magnetic reconnection can occur in magnetized plasmas when magnetic flux is transported between different plasmas, often with conversion of part of the magnetic energy to thermal, kinetic or wave energy. This will happen in the Earth's magnetosphere, see for example the *neutral point* in figure 1.

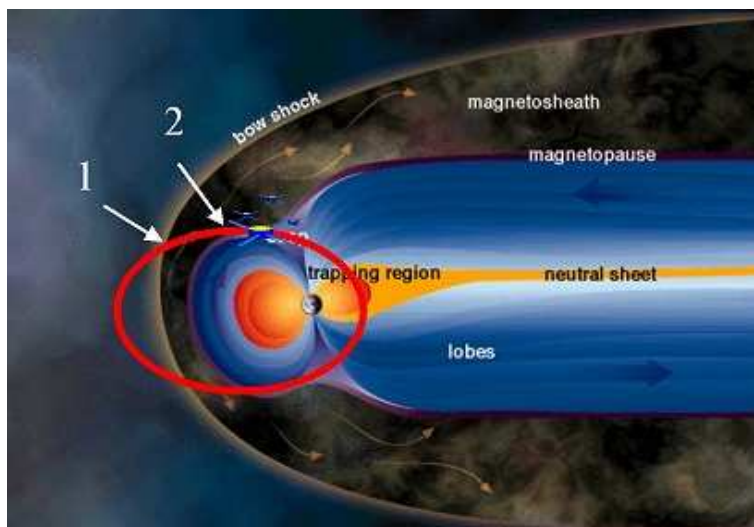


Figure 3: The orbit of the four Cluster satellites (from <http://sci.esa.int>). Two of the key regions for the Cluster mission are pointed out: 1. The bow shock. 2. The magnetopause.

and conceptually simple technique of two spherical probes measuring the potential difference in the plasma. The probes are separated by 88 m wire booms and are deployed radially by the spinning energy of the spacecraft. (Since the probes are confined in the spin plane, the data from EFW provides only information about the component of the electric field in this plane.) The probes are 8 cm in diameter and the diameter of the wire booms is 2.2 mm. Each of the satellites carries two pairs of probes with the booms perpendicular to each other, to be able to measure the electric field up to high frequencies. As has been mentioned, Cluster will get a positive potential on orbit (normally around 5-30 V). Unless special measurements are taken, the probes will reach the same potential as the spacecraft, which means that the measurements will be affected. To reduce the probe potential to values close to the potential in the surrounding plasma, a bias current between the spacecraft and the probe has to be applied. This will bring the potential of the probes to around +1 V relative to the plasma. If the local plasma conditions are the same around both probes, the electric field in the plasma can be measured using the potential difference between the probes (see figure 4). Close to the probes there is an element at negative potential, called *guard*, intended to prevent asymmetric currents of photoelectrons to the booms and too much influence from the boom potential. More information about the operational principle of EFW can be found in [17].

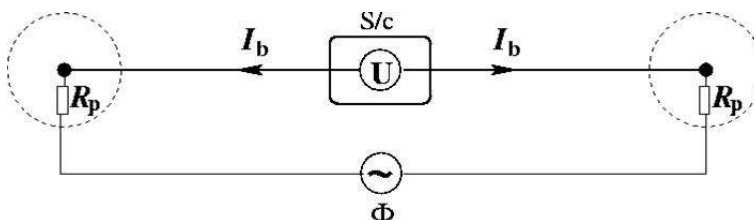


Figure 4: The Electric Fields and Waves instrument, EFW (from [1]). A bias current between the spacecraft and the probes will reduce the potential of the probes. If the plasma conditions, especially the resistance R_p , close to the two probes are equal, the potential in the plasma, Φ , will be identical to the potential measured by the spacecraft, U . The spacecraft can thus be compared to a voltmeter.

Electron drift instruments are based on a technique determining the drift of high-

energetic electrons in a magnetized plasma (see figure 5). Two beams of keV electrons are emitted from electron guns on the spacecraft. If a sufficiently strong (at least 30 nT) magnetic field is present, the electrons will experience a magnetic force strong enough to make it possible to regain the electrons at detectors on the spacecraft. The electrons will also feel a force from the electric field in the plasma, which will lead to a drift of the electrons at a velocity of $\mathbf{E} \times \mathbf{B}/B^2$ (see section 2.2). Detecting this drift from the two electron beams, the electric field can be extracted from magnetic field data.

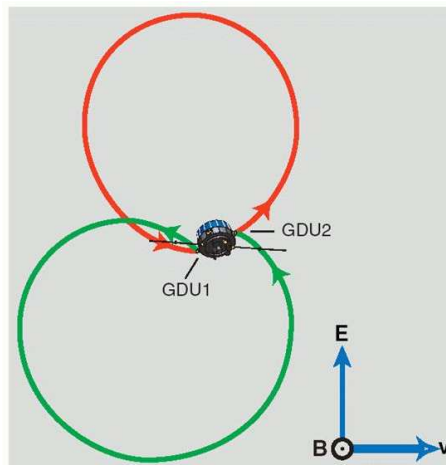


Figure 5: The Electron Drift Instrument uses the drift of electrons in a magnetized plasma to measure the electric field. Two high energetic electron beams are emitted from the spacecraft to measure the drift (from [16]).

Both of the instruments experience problems in some regions of the magnetosphere. Fortunately, the problems occur in different regions for the two instruments, making them complement each other well. An extensive comparison between EDI and EFW has recently been carried out by Eriksson et al. [1]. Parts of this treatment, as well as a discussion on the problems experienced with EFW, is also presented in [18]. In short, EDI will evidently not function for too weak magnetic fields. It will also have problems for rapidly varying magnetic and electric fields, which can be encountered in the aurora regions for example. In these regions, EDI often also have problems with naturally accelerated auroral electrons of keV energy swamping the EDI detectors, thus making it impossible to identify the emitted beam electrons. EFW will have no problems in regions, due to the construction with two spinning crossing booms, which allow high frequency measurements. On the other hand, EFW measurements can be affected by the influence of the positive potential of the satellite on the plasma environment. This is especially the case in cold, tenuous plasmas, existing for example in the polar caps, where the up-streaming polar wind is dominant. In figure 6 electric field data from Cluster in the polar cap at a geocentric distance of $8.6 R_E$ is shown. In the upper panel the spacecraft potential is displayed, while the two lower panels show the electric field components E_x and E_y for EDI (blue) and EFW (red). The component E_x is almost aligned with the magnetic field lines, in the direction of the polar wind. E_y is perpendicular to E_x and consequently also roughly perpendicular to the polar wind. As can easily be seen, the measurements from EFW is mainly disturbed for E_x , thus in the direction of the polar wind. The errors also grow when the spacecraft potential increases. These two facts provide evidence for an enhanced wake behind the spacecraft, creating the spurious electric field in the EFW data.

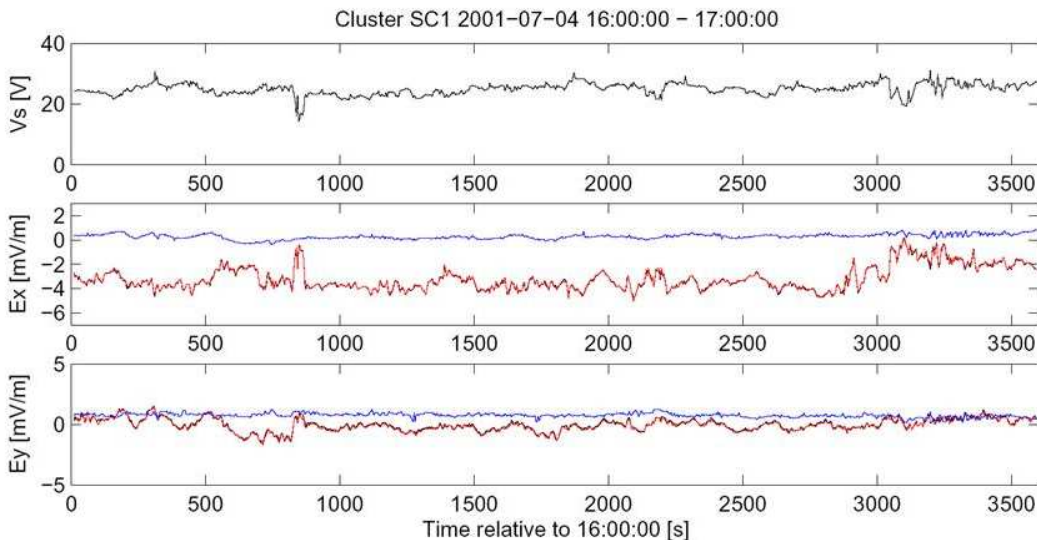


Figure 6: Electric field data from the polar cap at a geocentric distance of $8.6 R_E$. The upper panel shows the spacecraft potential and the two lower panels show comparisons between two components of the electric field measured by EFW (red) and EDI (blue). E_x is in this case approximately aligned with the direction of the polar wind, while E_y is roughly perpendicular to this direction. EFW experiences problems mainly in the E_x -direction, when the spacecraft potential is high.

3.3 Enhanced wake formation behind Cluster

To understand the problems for EFW, we should investigate how a wake forms in a flowing plasma. A necessary condition for wake formation is that the flow is *supersonic* with respect to the ions, i. e. the flow kinetic energy of the ions, E_k^i , exceeds their thermal energy, KT_i . When an object is placed in a supersonic ion flow, a wake void of ions will be created behind the object. This arises from the fact that the spacecraft is acting as an obstacle to the flowing ions, and since their thermal speed is lower than the speed of the flow, the cavity will not be filled immediately. Figure 7 gives a schematic illustration of this phenomenon. If the flow is not only supersonic for the ions, but also *subsonic* for the electrons ($E_k^e < KT_e$), the electrons will be able to access the wake region, thus giving rise to a negatively charged wake behind the spacecraft⁷. This is the case for the flow in the polar wind, but also in the dense solar wind, where wakes normally have been studied. The high plasma density in the solar wind makes it different from the tenuous polar wind, however, since it will ensure a low spacecraft potential. As has been shown by Pedersen [19] [20], the spacecraft potential depends strongly on the plasma density: a high plasma density translates to low positive spacecraft potentials, whereas a low density corresponds to high positive potentials. Thus, in the solar wind the spacecraft potential, V_s , will not exceed the ion flow energy, E_k^i ($eV_s < E_k^i$). Therefore the ions will not be deflected by any spacecraft potential, but will see the spacecraft body only as the obstacle.

For the Cluster case, we have to study wake formation in the polar wind. An interesting feature of this region is that the up-flowing plasma is so tenuous that the spacecraft potential will exceed the ion kinetic energy, which means that the ions will be prevented from reaching the spacecraft. The polar wind ions thus obey the following inequality:

⁷If the thermal energy of the electrons is close to the ion kinetic energy, the negative charge will affect the motion of the ions considerably, thus changing the shape of the wake.

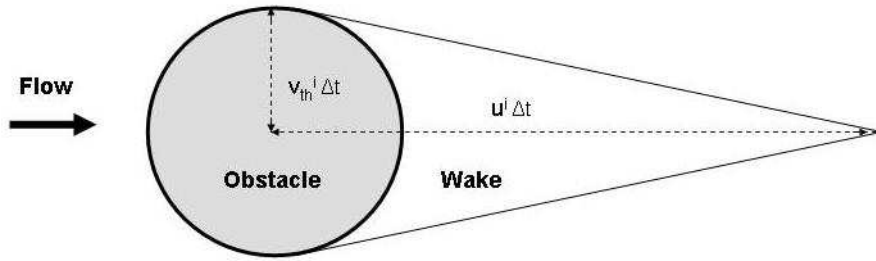


Figure 7: Schematic picture of a wake, where $eV_s < E_k^i$. The speed of the ion flow is higher than the ion thermal speed, which will lead to a region void of ions behind the obstacle. The time Δt is the time for the ions to fill the space behind the obstacle due to their thermal speed, v_{th}^i . In this time the ions will travel a distance $u_i \Delta t$ in the flow direction, where u_i is the flow speed. This process will cause the wake behind the spacecraft. If the electrons are subsonic, they will fill the wake, which will obtain a negative net charge.

$$KT_i < E_k^i < eV_s \quad (5)$$

This means that the potential structure, rather than the physical shape of the spacecraft, will act as an obstacle for the ions. Moreover, the ions will be deflected by the spacecraft potential like in Rutherford scattering. These two factors will enhance the wake behind the spacecraft body (see figure 8). What is even more important, is that the thin wire booms, which are at the same potential as the spacecraft itself, will be able to cause a wake. The booms with a diameter of 2.2 mm will create no detectable wake effect when the spacecraft potential is low, as for example in the solar wind. However, for the polar wind, where the potential is higher than the ion kinetic energy their effective size⁸ will grow from millimeters to meters making them large obstacles for the flowing plasma. A large negatively charged wake will therefore be formed behind the spacecraft with its booms, which will affect the double-probe instrument: the probe in the downstream direction will be closer to the wake, thus detecting a lower potential than the upstream probe, giving rise to a spurious electric field. This is what happens in situations like in figure 6.

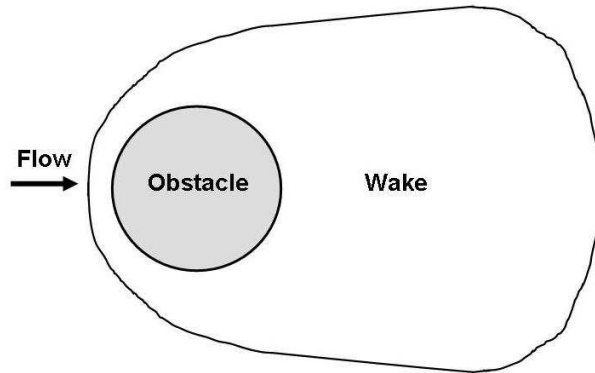


Figure 8: Schematic picture of an *enhanced* wake. The ions are deflected by the positive potential of the spacecraft, which is higher than the kinetic energy of the ions ($eV_s > E_k^i$). As for the wake in figure 7, this wake will be negatively charged, if the electrons are subsonic.

For more details on the formation of enhanced wakes, see [18], where some rough

⁸With *effective size* we mean the size of the obstacle preventing the ions to pass. For low potentials the effective size equals the physical size, but for a potential exceeding the ion kinetic energy, it can be approximated by the potential contour, where $e\Phi = E_k^i$.

estimations of the size of the enhanced wake also have been made. These estimations show that the wake may indeed cause spurious electric fields with magnitudes as large as those observed in EFW data. However, to get a more quantitative picture of the wake and the impact on the double-probe instrument, numerical simulations are needed. This is the subject of the two following sections.

4 Numerical simulations with *PicUp3D*

For modelling of the wake effect for Cluster, we use the open source simulation code package PicUp3D [21]. This package was developed in the framework of the IPICSS project (*Investigation of Plasma Induced Charging of Satellite Systems*), initiated at IRF-K⁹, with Julien Forest as main author. To obtain portability and possibility of development in community, the code is written in JAVA using only existing open source software for pre- and post-processing¹⁰. PicUp3D implements the Particle-In-Cell method (PIC), modelling both ions and electrons to solve different electrostatic spacecraft-plasma interaction problems.

The relevant set of equations describing electrostatic interactions in a plasma is the *Vlasov-Poisson system*, which is a kinetic description of the evolution of a system of plasma particles affected by self-consistent electric fields:

$$\left\{ \begin{array}{ll} \frac{\partial f_\alpha}{\partial t} + \mathbf{v}_\alpha \cdot \nabla f_\alpha + \mathbf{a}_\alpha \cdot \nabla_{\mathbf{v}_\alpha} f_\alpha = 0 & \text{The Vlasov equation} \\ \nabla^2 \Phi = -\frac{\rho}{\epsilon_0} & \text{The Poisson equation} \\ \mathbf{a}_\alpha = \frac{q_\alpha}{m_\alpha} (\mathbf{E} + \mathbf{v}_\alpha \times \mathbf{B}) \\ \mathbf{E} = -\nabla \Phi \\ n_\alpha = \int_{-\infty}^{\infty} f_\alpha(\mathbf{r}_\alpha, \mathbf{v}_\alpha, t) d^3 v_\alpha \\ \rho = \sum_\alpha q_\alpha n_\alpha \end{array} \right. \quad (6)$$

The unknown $f_\alpha = f_\alpha(\mathbf{r}_\alpha, \mathbf{v}_\alpha, t)$ is the distribution function for the species α (electrons or ions), which depends on the position vector, \mathbf{r}_α , the velocity, \mathbf{v}_α , and time, t . ∇_v is the gradient with respect to velocity, \mathbf{a}_α the acceleration and Φ the electric potential. q_α and m_α are the charge and the mass of the species α , respectively. For simplicity, we are considering the electrostatic case only, why the magnetic flux density, \mathbf{B} , is constant. The number densities, n_α , are obtained by integrating the different f_α over the entire velocity space and the charge density is the sum of the products of the number density and the corresponding charge. In the Vlasov equation collisions are neglected, since they are negligible compared to the electrostatic forces.

To solve the Vlasov-Poisson system numerically in the six-dimensional phase space is indeed possible, but requires both long computational times and much memory [22]. Therefore other approaches are often used for numerical simulations. One of the most common models is the PIC model [23], which traces the motion of plasma particles interacting with self-consistently computed electric and magnetic fields. To obtain reasonable computational times, the model does not integrate the trajectories of real plasma particles, but of *macro-particles*, which consist of millions of real particles of the same type in a certain velocity range. The mass of a macro-particle, M_α , is the sum of all individual masses of the plasma particles constituting the macro-particle. Similarly, the charge, Q_α , of the macro-particles is obtained. The total number of physical particles in the computational box is fixed by the nominal plasma density,

⁹Institutet för rymdfysik, Kiruna (Swedish Institute of Space Physics, Kiruna)

¹⁰In this project, MATLAB is used for post-processing instead of Gnuplot, for reasons of convenience.

while the number of macro-particles, N_{macro} , can be varied for reasons of either accuracy or low computational times. Since the equation of motion has to be solved for each macro-particle, the computational times will increase with more macro-particles. On the other hand, the numerical noise gets important with fewer macro-particles. To achieve a reasonable accuracy in our simulations, we adjust the number of macro-particles so that there are in average 8 macro-particles per computational cell. This results in an acceptable noise with a standard deviation of less than 5% for the ion and electron densities. The numerical noise could be reduced further by increasing the number of macro-particles, but it is proportional to $1/\sqrt{N_{\text{macro}}}$ and will therefore decrease slowly as N_{macro} , and thus the computational times, increase [24].

The motion of the macro-particles is determined by the following system of equations:

$$M_\alpha \frac{d\mathbf{v}_n}{dt} = Q_\alpha (\mathbf{E} + \mathbf{v}_n \times \mathbf{B}) \quad (7)$$

$$\frac{d\mathbf{r}_n}{dt} = \mathbf{v}_n \quad (8)$$

$$\nabla^2 \Phi = -\frac{\rho}{\epsilon_0} \quad (9)$$

$$\mathbf{E} = -\nabla \Phi \quad (10)$$

The equation of motion (7) and the velocity equation (8) are integrated for each of the macro-particles ($n = 1 \dots N_{\text{macro}}$), using a *leap-frog method* [23]:

$$M_\alpha \frac{\mathbf{v}_n^{\text{new}} - \mathbf{v}_n^{\text{old}}}{\Delta t} = Q_\alpha (\mathbf{E}^{\text{old}} + \mathbf{v}_n^{\text{old}} \times \mathbf{B}) \quad (11)$$

$$\frac{\mathbf{r}_n^{\text{new}} - \mathbf{r}_n^{\text{old}}}{\Delta t} = \mathbf{v}_n^{\text{new}}, \quad (12)$$

which yields

$$\mathbf{v}_n^{\text{new}} = \mathbf{v}_n^{\text{old}} + \Delta t \frac{Q_\alpha}{M_\alpha} (\mathbf{E}^{\text{old}} + \mathbf{v}_n^{\text{old}} \times \mathbf{B}) \quad (13)$$

$$\mathbf{r}_n^{\text{new}} = \mathbf{r}_n^{\text{old}} + \Delta t \mathbf{v}_n^{\text{new}} \quad (14)$$

A great advantage of the low-order leap-frog method is that it requires a minimum of operations and storage, which will reduce the computational times significantly compared to higher-order methods. In addition, it is still accurate to second order in Δt [23].

The differential equations for the fields ((9) and (10)) are solved using finite difference methods on a homogeneous three-dimensional Cartesian grid:

(9) \Rightarrow

$$\begin{aligned}
& \frac{\Phi^{i+1,j,k} - 2\Phi^{i,j,k} + \Phi^{i-1,j,k}}{(\Delta x)^2} + \\
& + \frac{\Phi^{i,j+1,k} - 2\Phi^{i,j,k} + \Phi^{i,j-1,k}}{(\Delta y)^2} + \\
& + \frac{\Phi^{i,j,k+1} - 2\Phi^{i,j,k} + \Phi^{i,j,k-1}}{(\Delta z)^2} = -\frac{\rho^{i,j,k}}{\epsilon_0}
\end{aligned} \tag{15}$$

(10) \Rightarrow

$$\begin{cases} E_x^i = \frac{\Phi^{i+1,j,k} - \Phi^{i-1,j,k}}{2\Delta x} \\ E_y^j = \frac{\Phi^{i,j+1,k} - \Phi^{i,j-1,k}}{2\Delta y} \\ E_z^k = \frac{\Phi^{i,j,k+1} - \Phi^{i,j,k-1}}{2\Delta z} \end{cases} \tag{16}$$

Equation (15) can be written in matrix form as:

$$C\Phi = -\frac{\rho}{\epsilon_0}, \tag{17}$$

where C is the coefficient matrix, and Φ and ρ are the ordered potential and charge density vectors, respectively

$$\begin{aligned}
\Phi &= [\Phi^{1,1,1}, \dots, \Phi^{N_x,1,1}, \Phi^{1,2,1}, \dots, \Phi^{N_x,N_y,1}, \Phi^{1,1,2}, \dots, \Phi^{N_x,N_y,N_z}]^T \\
\rho &= [\rho^{1,1,1}, \dots, \rho^{N_x,1,1}, \rho^{1,2,1}, \dots, \rho^{N_x,N_y,1}, \rho^{1,1,2}, \dots, \rho^{N_x,N_y,N_z}]^T
\end{aligned}$$

N_x , N_y and N_z are the number of grid points in each direction. PicUp3D solves the matrix equation using the *Gauss-Seidel method with Chebyshev convergence acceleration* [25]. For this solution the present charge density is needed at a specific grid point, $\rho^{i,j,k}$. This charge density has to be interpolated from the positions of the different charged macro-particles. The nearest-grid-point interpolation (NGP), which assigns all of the charge of a macro-particle to the nearest grid point, is the easiest interpolation method, but it is also least accurate. In the PIC method, the charge from the macro-particle is distributed over the closest grid-points. This is illustrated in figure 9 for a two-dimensional computational box.

The contributions from the charge q to the total charge distribution at the different grid points of the computational cell in figure 9 are given by

$$\begin{aligned}
\rho_q^{i,j} &= q \frac{A_{i,j}}{A_{\text{tot}}} \\
\rho_q^{i+1,j} &= q \frac{A_{i+1,j}}{A_{\text{tot}}} \\
\rho_q^{i,j+1} &= q \frac{A_{i,j+1}}{A_{\text{tot}}} \\
\rho_q^{i+1,j+1} &= q \frac{A_{i+1,j+1}}{A_{\text{tot}}}
\end{aligned} \tag{18}$$

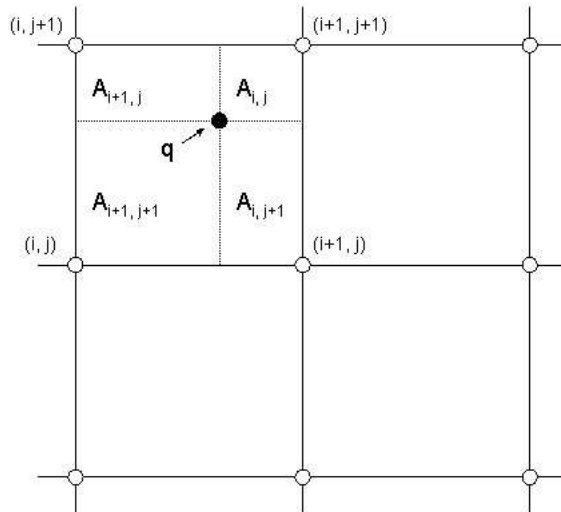


Figure 9: The PIC method interpolates the charge density at each discrete grid point using weights. In this two-dimensional case the contribution from the charge q to the total charge distribution at point (i, j) is $\rho_q^{i,j} = q \frac{A_{i,j}}{A_{\text{tot}}}$.

where A_{tot} is the total area of a computational cell, $A_{\text{tot}} = A_{i,j} + A_{i+1,j} + A_{i,j+1} + A_{i+1,j+1}$. Extending this method to three dimensions, the code uses partial volumes instead of areas and the charge is distributed over the eight closest grid points (the grid points constituting the cube in which the macro-particle is situated). Regarding the electric field, equation (16) gives the values at the grid points, whereas they have to be known at the position of the macro-particles to make it possible to solve the equation of motion (7). To achieve this, the interpolation method for the charge density is reversed. For the two-dimensional case, the electric field at the position of the macro-particle, \mathbf{r}_q , is given by

$$\mathbf{E}(\mathbf{r}_q) = \mathbf{E}_{i,j} \frac{A_{i,j}}{A_{\text{tot}}} + \mathbf{E}_{i+1,j} \frac{A_{i+1,j}}{A_{\text{tot}}} + \mathbf{E}_{i,j+1} \frac{A_{i,j+1}}{A_{\text{tot}}} + \mathbf{E}_{i+1,j+1} \frac{A_{i+1,j+1}}{A_{\text{tot}}} \quad (19)$$

The PIC method can now be summarised in the following scheme:

1. Move the macro-particles according to the old values for the electric field:
 - (a) Get the new velocity, $\mathbf{v}_n^{\text{new}}$, from equation (13).
 - (b) Solve equation (14) for the new position of the macro-particle, $\mathbf{r}_n^{\text{new}}$.
2. Calculate the charge density at each grid point from the positions of the macro-particles using the PIC interpolation method (equation (18)).
3. Solve the matrix form of equation (15) to get the potential at each grid point.
4. Obtain new values for the electric field at each grid point using equation (16).
5. Interpolate the values for the electric field at the positions of the macro-particles (equation (19)).
6. Restart at 1.

This loop has to be carried out for each of the macro-particles, which explains why the computational times grow bigger as the number of macro-particles increases. The time-step and the mass ratio between electrons and ions will also influence the computational times. We chose the time-step in such a way that $\max(v_{\text{th}}^e, v_{\text{th}}^i, u_e, u_i)\Delta t \ll \Delta r$, so that no particle will cross a cell in less than a few time steps¹¹. In our simulations, v_{th}^e is the maximum velocity and we use the time-step $v_{\text{th}}^e \Delta t = 0.2\Delta r$. The current edition of PicUp3D models only one species of ions and the nominal mass ratio between the ions and electrons is set to $m_i/m_e = 100$. The mass ratio is chosen to be small in order to reduce the convergence time¹² of the simulation: with a smaller mass ratio the ions are moving faster and equilibrium is thus established faster. Previous simulations with other codes, e.g. the code by Singh et al. [26], have shown that the value of the mass ratio has no great influence on the final results for non-flowing plasmas. In which way the mass ratio will affect the final results for a flowing plasma simulated in PicUp3D, is discussed in section 5.3.1.

The treatment of the boundary conditions and the injection and loss of macro-particles at the boundary are crucial for the performance of the code. The macro-particles are injected and lost through the boundary using a method of *virtual tanks*, described in more details in [21] and [26]. In the tanks, which are connected to each of the walls of the computational box, the macro-particles are spread uniformly according to the nominal plasma density and follow a Maxwellian distribution with the nominal electron and ion temperatures. Since no fields are applied in the tank, the macro-particles can scatter freely in and out through the boundary, thus defining an open boundary. For the potential, Dirichlet boundary conditions ($\Phi_b = 0$) are chosen. These boundary conditions have a great advantage in the easy implementation, but need special care not to influence the derivation of the potential in the rest of the computational box. This means that the walls of the computational box have to be sufficiently far away from the spacecraft; the larger the box is, the less influence the boundary conditions will have. However, since the computational time will increase when the size of the box increases, our ambition is to find a minimum value of the distance between the spacecraft and the walls. Theoretically, the walls should not be closer to the spacecraft than a few λ_D , in order to let the Debye shielding decrease the potential to a satisfactorily low level. To check this assumption, the influence of the Dirichlet boundary conditions for different sizes of computational boxes has been studied numerically (see section 5.3.1). On the inner boundary, at the spacecraft border, the potential is set as an input parameter, and is not calculated self-consistently. The fixed spacecraft potential is of no concern in our case, as Pedersen [19] has extracted a density-potential relation for Cluster from data. We can thus choose a potential which is consistent with this relation.

All the input parameters are given in dimensionless units, normalized to characteristic scales of the plasma (for length for example we use the Debye length as characteristic scale and for the potential we use the thermal energy of electrons). Consequently, the equations (7)-(10) in the numerical implementation also have to be scaled. Other physical input parameters than the spacecraft potential are the number of macro-particles, the size of the computational box in grid points and in Debye lengths, the number of particles per macro-particle, the *magic number*¹³, the magnetic flux density,

¹¹ Δr represents the spatial steps Δx , Δy and Δz .

¹²In this context, we refer to *convergence time* as the simulation time to achieve steady state of the physical system.

¹³The magic number, called so for historical reasons, is one over the number of particles in a Debye sphere, i. e. $\frac{1}{N_D} = \frac{1}{\lambda_D^3 n_0}$. The number of particles in a Debye sphere has to be sufficiently large for Debye shielding to take place. Therefore, the notion of collective behaviour for plasmas requires that ($N_D \gg 1$) [7].

the relative spacecraft velocity expressed in the thermal velocity of the electrons, the time-step in plasma periods (ω_{pe}^{-1}), the spacecraft geometry and finally the mass ratio between electrons and ions.

Thus, important plasma parameters as the plasma density and the electron temperature¹⁴ are not defined explicitly, but are determined implicitly by some of the input parameters. The output parameters can to some extent be chosen from what kind of phenomena that is to be studied, but also from such limitations as computational time and disk space. In our study the most important output has been the potential and the ion and electron densities.

The computational grid in PicUp3D is rectangular and homogeneous for reasons of simple implementation. Such a grid can, however, be problematic, since the grid-size should be small to catch the details of the spacecraft-plasma interactions. On the other hand, the computational box has to be sufficiently large due to the impact on the potential distribution of the Dirichlet boundary conditions. For a detailed description a large number of computational cells is therefore needed, which leads to long computational times. Thus, the grid-size has to be chosen as a compromise between the requirement of a detailed description and reasonable computational times.

PicUp3D is designed to be used on common workstations rather than on supercomputers to facilitate the use by engineers and scientists, being able to run it on their own PCs. We have run our simulations using FreeBSD on common PCs (2.8 GHz) with around 1.6 GB of RAM allocated to the simulation. In the largest simulations (such as the two first presented simulations below) more than 4 million macro-particles have been used, and they have taken around five days to complete.

¹⁴In the current release of PicUp3D the ions and electrons are assumed to have the same temperature.

5 Simulations of the Cluster phenomena

A number of simulations have been carried out to examine the effect of the wake on the double-probe electric field instrument. Detailed results are presented for two of the simulations with different spacecraft geometries, but with the same plasma parameters. In the first simulation the spacecraft is modelled as a single boom, neglecting the effects of the spacecraft body (see figure 10), while the other simulation investigates the effects of the spacecraft body itself. This is partly done to simplify the computational problem, but it is also interesting to see how much the different parts of the spacecraft affect the wake structure. A great advantage of simulating only the spacecraft body, is also that we do not have to fix the angle of the booms, thus getting a picture of the electric field measurements for a large range of angles from the same simulation. In the rest of the simulations, we use either one of these two spacecraft geometries, but vary the plasma parameters, as well as the size of the computational box. For the two nominal simulations we use the following plasma parameters:

- Plasma density, $n_0 = 0.20 \text{ cm}^{-3}$
- Electron temperature, $KT_e = 2.0 \text{ eV}$
- Ion temperature, $KT_i = 2.0 \text{ eV}$
- Ion drift kinetic energy, $E_k^i = 10 \text{ eV}$
- Magnetic field, $B = 100 \text{ nT}$

These properties are consistent with the conditions derived from the POLAR satellite data by Su et al. [6] as well as with the Cluster observations in figure 6. The Debye length becomes $\lambda_D \approx 24 \text{ m}$ and the electron plasma frequency $\omega_{pe}/2\pi \approx 4 \text{ kHz}$. The ion drift flow is taken to be in the positive y-direction. We use the nominal mass ratio of $m_i/m_e = 100$, which means that the kinetic energy corresponds to the following flow velocity for ions

$$u = \sqrt{\frac{2E_k^i}{m_i}} = \sqrt{\frac{2 \times 10 \times q_e}{100m_e}} = 190 \text{ km/s}, \quad (20)$$

which is much higher than the flow velocity of 44 km/s we would get for protons using the real mass ratio. This is of less concern to us, since the energy of the particles is conserved along their trajectories, which means that we will probably get a relatively correct picture of the wake structure even with a small mass ratio. What is important for enhanced wake formation is, as mentioned above, that the flow velocity obeys the inequality

$$KT_i < E_k^i < eV_s, \quad (21)$$

which is satisfied also with a mass ratio of $m_i/m_e = 100$. Moreover the flow should still be subsonic compared to the electrons. For the simulation input the flow velocity should be expressed in thermal velocities, which in PicUp3D is defined as $\sqrt{KT/m}$. Using $E_k^i = \frac{m_i u^2}{2}$, we get

$$u = \sqrt{2 \frac{E_k^i}{KT_i}} v_{th}^i = \sqrt{2 \frac{E_k^i}{KT_e} \frac{m_e}{m_i}} v_{th}^e = \sqrt{10} v_{th}^i = \frac{1}{\sqrt{10}} v_{th}^e. \quad (22)$$

This means that the requirement on the flow to be supersonic for ions ($u > v_{\text{th}}^i$) and subsonic ($u < v_{\text{th}}^e$) for the electrons is satisfied. There will thus be an ion wake behind the spacecraft, which will be filled with electrons due to their large mobility.

In all the simulations the weak magnetic field of 100 nT is neglected, as the Larmor radii for the two dominant ion species in the polar wind (H^+ and O^+) are significantly larger than the scale of the problem and the simulation boxes. The Larmor radius is

$$r_L = \frac{v_{\text{th}}}{\omega_c} = \frac{\sqrt{KTm}}{|q|B}. \quad (23)$$

For O^+ the Larmor radius is 5.8 km and for H^+ 1.4 km. The electron Larmor radius of 34 m is closer to the scale of the problem, but has also been neglected. This may possibly cause some overestimation of the electron densities in the wake. Since the flow of electrons is subsonic, this problem should, however, be small. For simplicity, in none of the cases the satellite is assumed to emit photoelectrons. This approximation can be justified by the high potential of the spacecraft (25 – 35 V) indicated in figure 6, since it will recollect most of the emitted photoelectrons, which typically have energies of a few eV [20].

5.1 Booms only

For this specific run, the grid-size is $4 \times 4 \times 4 \text{ m}^3$ and the number of grid-steps in each direction is $N_x = 60$, $N_y = 120$, $N_z = 60$ (see figure 10). Thus, the dimensions of the computational box is $x = 240 \text{ m}$, $y = 480 \text{ m}$, $z = 240 \text{ m}$, which all may be compared to $\lambda_D = 24 \text{ m}$. The integration time step for the motion of the particles is set to $0.034 \omega_{\text{pe}}^{-1}$ in accordance with the discussion in section 4.

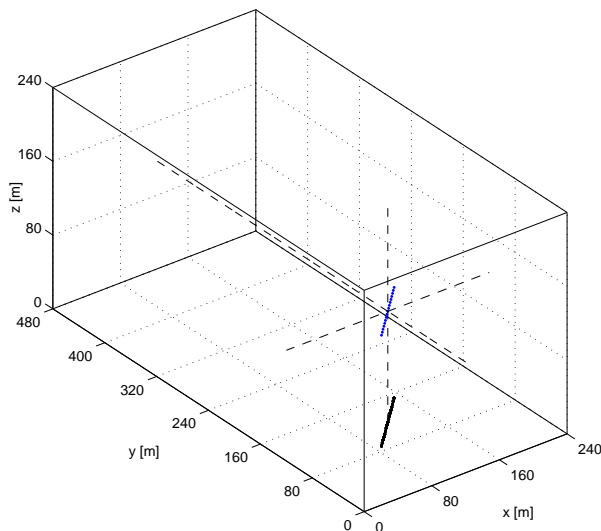


Figure 10: The boom in the computational box, which with the grid resolution of 4 m has the dimensions $x = 240 \text{ m}$, $y = 480 \text{ m}$, $z = 240 \text{ m}$. The length of the boom is 90.5 m and consists of 17 discrete grid points (blue). The black dotted line is the projection of the boom on to the plane $z=0$. The flow enters at $y = 0$.

The boom is placed in the xy -plane at $z = 120 \text{ m}$ at an angle of 45° relative to positive x -axis, which means that it has the same angle to the flow. This angle has been chosen as typical for the simulations with booms. As PicUp3D includes no explicit provisions for modelling booms, we have instead fixed the potential of 17 discrete grid points,

extending from $(x = 88 \text{ m}, y = 88 \text{ m})$ to $(x = 152 \text{ m}, y = 152 \text{ m})$. This means that the distance to the walls behind the boom is much larger than the distance in front of the boom, in order to avoid the Dirichlet boundary conditions affecting the wake structure. The boom in the simulations obtains a length of 90.5 m, close to the actual length 88 m. Each grid point on the boom is set to the potential +20 V. If we want to model situations like the data in figure 6, the potential of the spacecraft, and hence of the boom, should rather be 25 – 35 V. However, due to the grid resolution of 4 m, the decrease of the potential close to the boom is slower than expected from a real wire boom of 2.2 mm diameter, and it will be shown later in this report that the choice of 20 V for the grid points modelling the boom actually corresponds to a thin wire boom at around 35 V. This value is consistent with the situations in figure 6, and also with a plasma density of approximately 0.2 cm^{-3} [19].

Results from the boom simulations are shown in figures 11-13. The output data is averaged over the time period from $30 \omega_{pe}^{-1}$ to the end of the simulation at $60 \omega_{pe}^{-1}$ in order to obtain smoother plots. Figures 11 and 12 show the ion density and the potential around the boom in the planes $z = 120$, $x = 120$ and $y = 120$ respectively. The planes $x = 120$ and $y = 120$ both intersects the midpoint of the boom, and the plane $z = 120$ is the plane containing the grid points of the boom. As expected, there is a clearly visible wake in the ion density behind the booms (see figure 11). For the potential the dominating structure is the decaying potential around the boom, giving essentially elliptic equipotentials down to 1 V, which can be seen most clearly in figure 12(a). Behind the boom a negatively charged wake is formed, reaching a minimum potential of -0.80 V. In figures 12(b) and 12(c), the equipotentials close to the boom gets an elliptical shape due to the cut through the tilted boom. The most apparent effect on the density of electrons seen in figure 13 is their agglomeration around the positive boom. A small depletion in the region of the wake can also be seen, as is expected for a wake approaching Debye length scale. It should be noted that the ions, whose energy is around 10 eV, are not influenced by the details of a wake potential at a few tenths of volts. This means that the ion density in figure 11 results essentially from the potential of the booms, so that the ion density is only marginally affected by any possible influence from the Dirichlet boundary conditions on the potential.

We will now use the simulation result to quantify the impact of the wake field on a double-probe electric field instrument. Such an instrument has one probe at each end of the boom, with bootstrapped elements in between, which are intended to shield away the direct influence of the boom potential (see section 3.2). For Cluster EFW, the probes are 3 m outside the part of the wire booms which are at spacecraft potential. In figure 14(a), we plot the difference in potential between two probes which are at the same distance from the opposite ends of the wire boom, as a function the distance from the boom ends. The maximum potential difference is approximately 520 mV. One grid spacing distance (4 m) out from the boom on each side, which is close to the 3 m relevant for Cluster EFW, the observed potential difference between the probes is 460 mV. Dividing this by 90.5 m, we find that EFW could be expected to suggest an apparent electric field of 5 mV/m because of the wake. This is true for the simulated boom angle with respect to the positive x -axis of 45° . The amplitude of the perturbation should vary with this angle, reaching a maximum at 90° and 270° . Therefore, the wake induced field in data from the spinning spacecraft frame like in figure 6 could be expected to be somewhat larger, around 6 or 7 mV/m. These values are close to the observed EFW- EDI discrepancies in figure 6. We should, however, remember that the plot in figure 14(a) is based on a simulation with 4 m grid resolution. Such a resolution cannot possibly catch all details a few meters from the ends of the wire booms, but in as far as the difference results from the large scale properties of the wake, and not

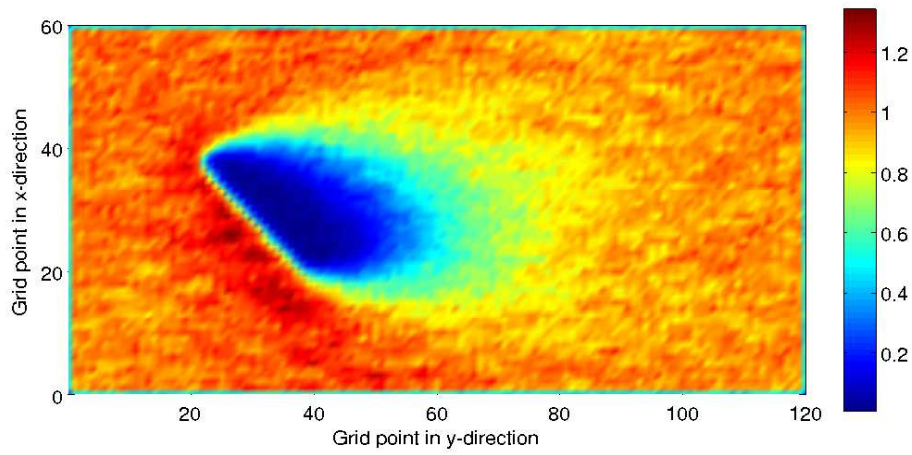
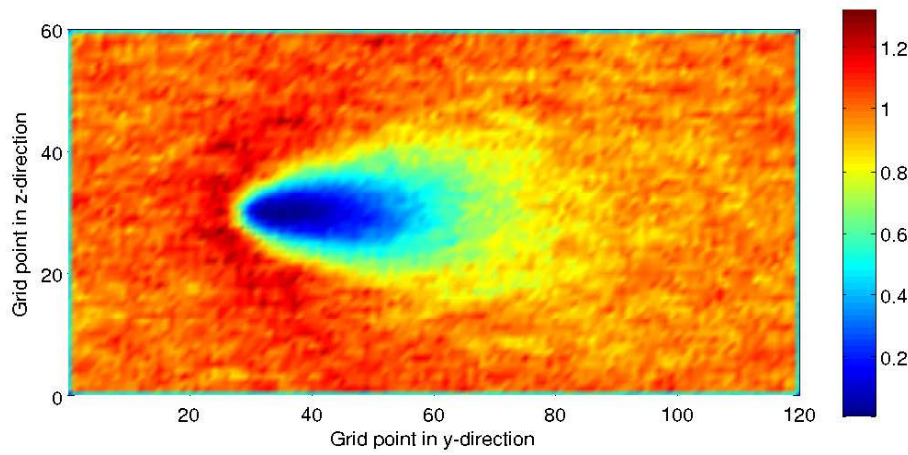
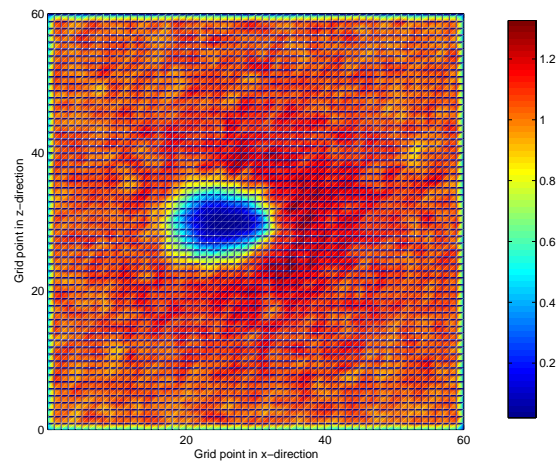
(a) Ion density in the xy-plane at $z = 120$ m.(b) Ion density in the yz-plane at $x = 120$ m.(c) Ion density in the xz-plane at $y = 120$ m.

Figure 11: Averaged normalized densities of ions from the boom simulation between $30 \omega_{pe}^{-1}$ and $60 \omega_{pe}^{-1}$ in different planes. (The grid spacing is 4 m.)

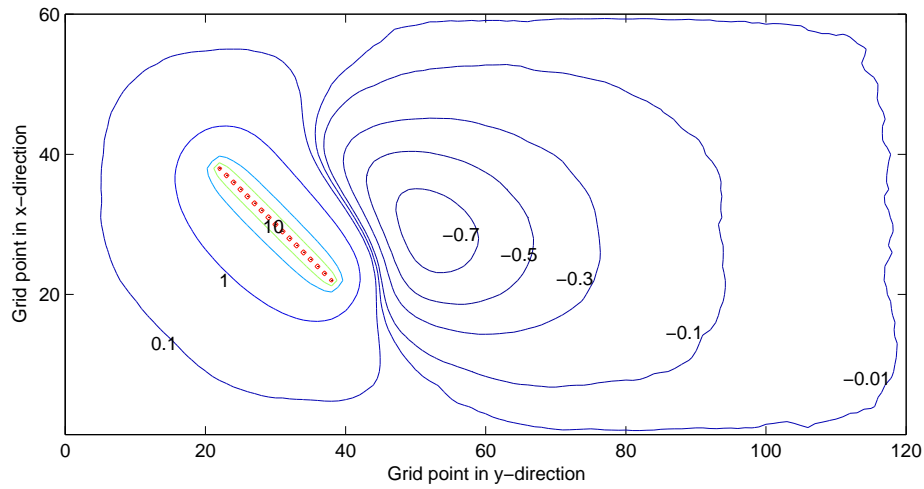
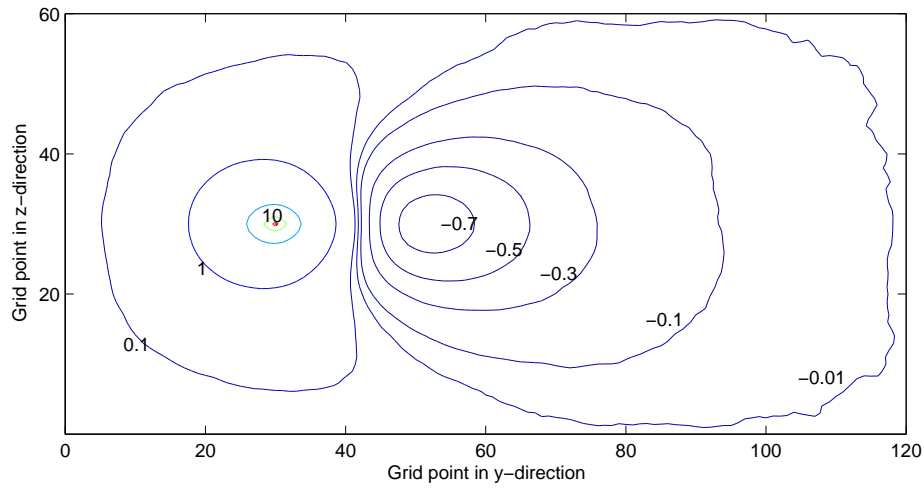
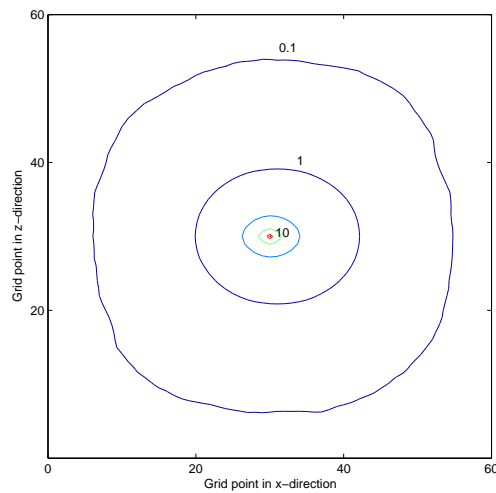
(a) Potential in the xy-plane at $z = 120$ m.(b) Potential in the yz-plane at $x = 120$ m.(c) Potential in the xz-plane at $y = 120$ m.

Figure 12: Averaged potential from the boom simulation between $30 \omega_{pe}^{-1}$ and $60 \omega_{pe}^{-1}$ in different planes. The minimum value of the potential in the wake is -0.80 V. Equipotential contours are given at -0.7 , -0.5 , -0.3 , -0.1 , -0.01 , 0.1 , 1 , 5 , 10 , 17 and 20 V. (The grid spacing is 4 m.)

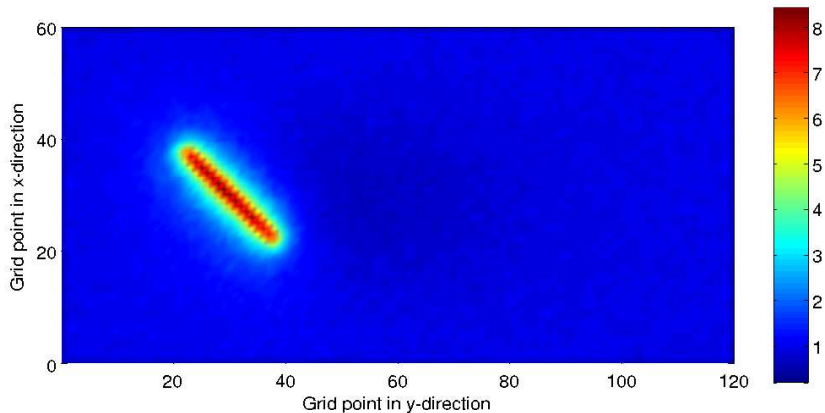


Figure 13: Averaged normalized density of electrons from the boom simulation between $30 \omega_{pe}^{-1}$ and $60 \omega_{pe}^{-1}$ in the xy -plane. (The grid spacing is 4 m.)

from the details close to the probe positions, we may expect the result to be reasonably correct.

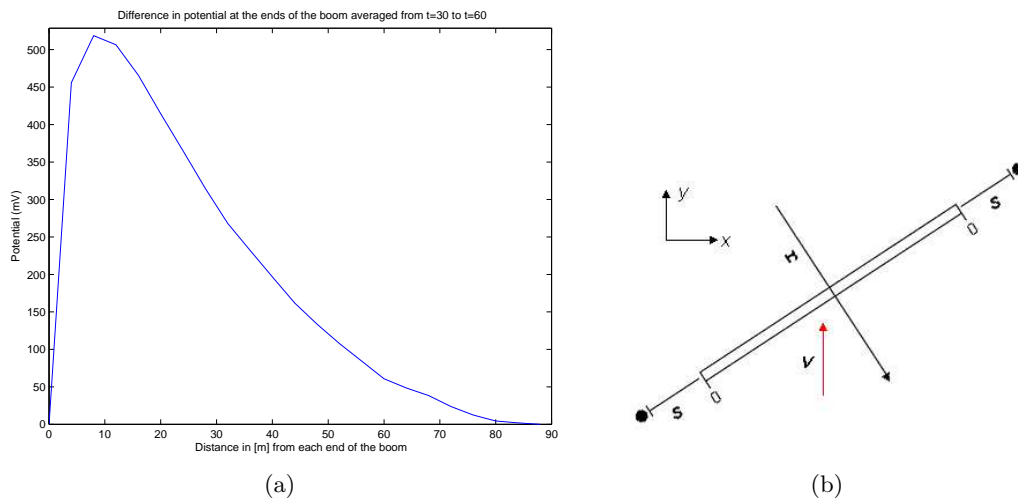


Figure 14: (a) Difference in potential between the ends of the boom. The maximum potential difference is 520 mV. (b) Schematic picture of the boom explaining the horizontal axis of (a): s is the distance from the boom end to the probe. The coordinate r is the radial distance from the midpoint of the boom used in figure 15.

As has been mentioned above, the grid spacing of 4 m will result in the potential close to the boom attaining larger values than would have been the case for a real wire boom (2.2 mm diameter for Cluster EFW) at 20 V. Several Debye lengths, and hence many grid steps, away from the boom, we may expect that the distance dependence on the potential is realistic, but close to the boom, the simulated potential will decay too slowly with distance. To compensate for this discrepancy, an effective boom potential is calculated by comparison with analytical models. At high potentials close to the boom the Debye shielding has only small effects and the boom potential can be compared to the vacuum potential of a thin cylinder. According to Hallén [27] [28], the vacuum potential of a thin cylinder at potential V is

$$\Phi(\hat{x}, \hat{y}, \hat{z}) = \frac{V}{2 \ln\left(\frac{l}{a}\right)} \ln\left(\frac{d - \hat{x} + r_1}{-d - \hat{x} + r_2}\right), \quad (24)$$

where l is the length of the cylinder which is aligned with the \hat{x} -axis and centred on the origin, a is its radius, $d = l/2$, $r_1 = \sqrt{(\hat{x} - d)^2 + \hat{y}^2 + \hat{z}^2}$ and $r_2 = \sqrt{(\hat{x} + d)^2 + \hat{y}^2 + \hat{z}^2}$. We now look for a value of V in this expression that results in a potential approximating the simulation result around 10 V and a few volts below, as this should be the most sensitive region for the dynamics of the ions, whose drift energy is 10 eV. In figure 15 the simulated potential (dashed blue) is plotted together with the analytic model for a thin boom potential of 35 V (black), with radial distance from the midpoint of the boom on the horizontal axis. It can be seen that this indeed approximates the simulated potential field around and below 10 V, and we may thus assume that the potential of 20 V applied to the point cluster simulating the booms corresponds to an actual potential as high as 35 V for a real wire boom.

Further away from the boom, equation (24) does not give a correct picture, because of the Debye shielding in the plasma. Therefore it is also adequate to compare the simulated boom potential to that of a Debye shielded infinite cylinder. To find the expression for the Debye shielded cylinder, we look at the linearized Poisson equation, which for $T_i = T_e$ takes the form

$$\nabla^2 \Phi = \frac{2}{\lambda_D^2} \Phi. \quad (25)$$

Normally, this equation is solved for spherical geometry with $\nabla^2 \Phi(r) = \frac{1}{r} \frac{d^2}{dr^2} (r\Phi)$. In this case, the geometry is, however, cylindrical symmetrical and $\nabla^2 \Phi(r) = \frac{1}{r} \frac{d}{dr} (r \frac{d\Phi}{dr})$. With requirements that the potential should vanish at infinity and equal the boom potential, V , at the radius of the boom, a , we get the following solution to the linearized Poisson equation:

$$\Phi(r) = V \frac{K_0 \left(\frac{r\sqrt{2}}{\lambda_D} \right)}{K_0 \left(\frac{a\sqrt{2}}{\lambda_D} \right)}, \quad (26)$$

where K_0 is a modified Bessel function of the second kind. The Debye shielded potential is plotted in figure 15 in red. As expected, the simulated potential and the shielded cylinder approach each other far from the boom. Closer to the boom, the Debye shielding expression (26) breaks down because of violation of the assumption $e\Phi \ll KT_e$ inherent in the linear Debye shielding law. The influence of the wake on the potential can clearly be seen in the asymmetry of the simulation data.

5.2 Spacecraft body without booms

We will now consider the second simulation, in which the spacecraft body is taken into account, while neglecting the booms. The size of the computational box and of the grid-size are the same as in the previous simulation, as well as the integration time step. With a 4 m grid the best approximation to the Cluster spacecraft body, which is cylindrical of height 1.5 m and diameter 2.9 m, is a cube with dimensions $4 \times 4 \times 4 \text{ m}^3$. We will return to the limitations of this model below. The cube is placed at the midpoint of the boom in the previous simulation and consists of 8 grid points¹⁵, one in each corner of the cube. We set the grid points to a potential of 16 V, taking the exaggerated size of the cube representing the spacecraft into account. The 16 V for

¹⁵The coordinates of the corners [m] are (120,120,120), (124,120,120), (124,124,120), (120,124,120), (120,120,124), (124,120,124), (124,124,124) and (120,124,124).

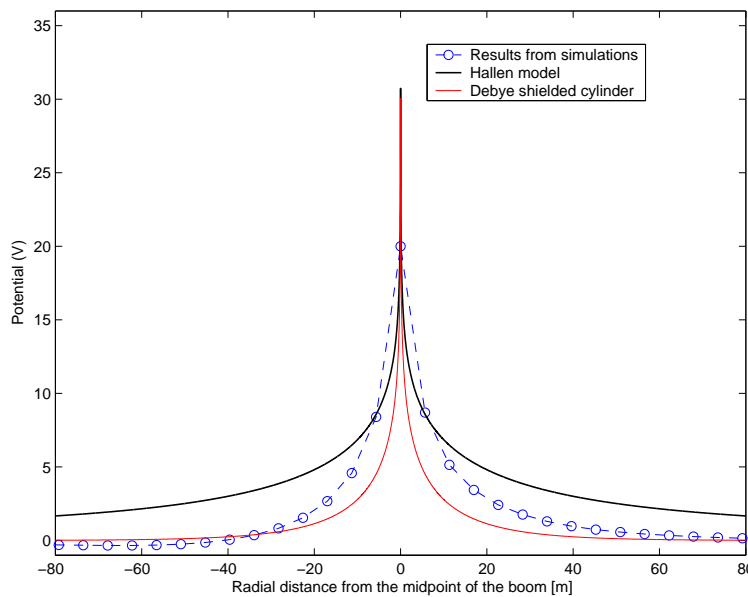


Figure 15: Comparison between the potential obtained from the simulation (dashed blue) and analytical models. The red line corresponds to an infinite Debye shielded cylinder and the black line to the model introduced by Hallén. The horizontal axis gives the radial distance from the center of the boom in the boom-flow plane (r in figure 14(b)).

the cube corresponds to an effective potential of 35 V for the spacecraft, i. e. the same value as for the booms, as will be shown below.

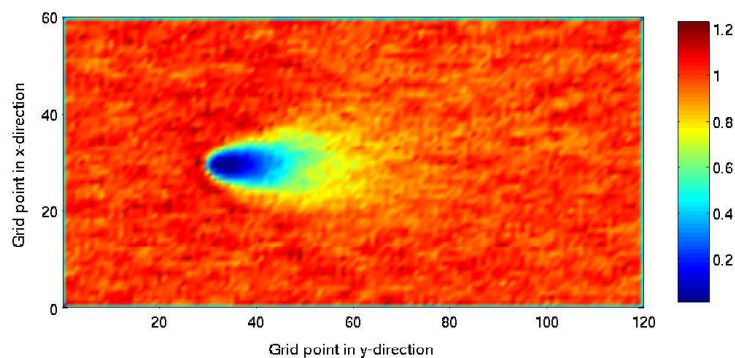


Figure 16: Averaged ion density from the cube simulation between $30 \omega_{pe}^{-1}$ and $60 \omega_{pe}^{-1}$ in the xy -plane. (The grid spacing is 4 m.)

In figures 16 and 17 the ion density and the potential in the xy -plane from the simulations are shown. The wake behind the cube is not surprisingly smaller than the wake behind the boom, reaching a minimum value of -0.34 V for the potential. This is much smaller than the value for the boom, but the minimum is closer to the spacecraft in this case and could therefore still affect the electric field instrument significantly. To get an estimate of the influence on the instrument we look at the potential difference between two points on opposite sides of the spacecraft separated by the boom length of 88 m. As has been mentioned, an advantage of neglecting the wake effects of the booms, is that we do not have to fix the angle of the booms relative to the flow. We can therefore plot the potential difference between the probes as a function of the angle of the virtual booms relative to the flow (see figure 18(a)). The potential at each ends of the booms is calculated using the PIC interpolation method described in section

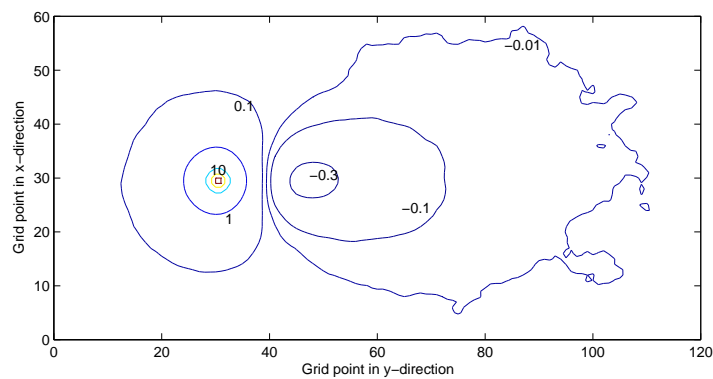


Figure 17: Averaged potential from the cube simulation between $30 \omega_{pe}^{-1}$ and $60 \omega_{pe}^{-1}$ in the xy -plane. The minimum value of the potential in the wake is -0.34 V. Equipotential contours are given at -0.3 , -0.1 , -0.01 , 0.1 , 1 , 5 , 10 and 16 V. (The grid spacing is 4 m.)

4. The maximum potential difference is around 520 mV/m, which yields a spurious electric field of approximately 7 mV/m.

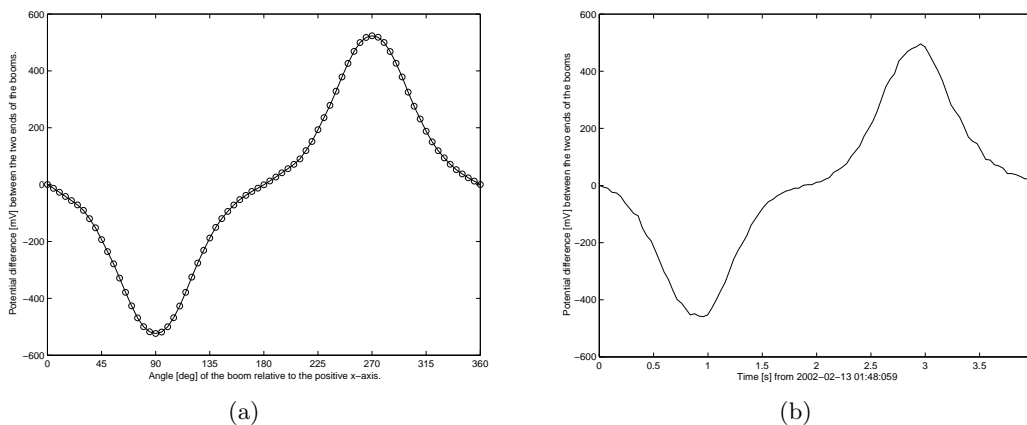


Figure 18: (a) Potential difference between the probes at different angles of the boom relative to the flow. The maximum potential difference is around 520 mV. (b) Measurement of the electric field from the pair of probes 34 of the EFW instrument on Cluster 3 during one spin period (4 s).

As expected, the plot in figure 18(a) is periodic with maximum differences at 90° and 270° relative to the positive x -axis and minimum differences at 0° , 180° and 360° . Plots with the same overall shape as in figure 18(a) can be found in measurements from the EFW instrument on Cluster. Figure 18(b) shows EFW data from the polar wind during one spin period at a certain time. Comparison between the simulation and data plots provides clarification of the previously unexplained inflection point in the satellite data. From the simulation it can be seen that this inflection point arises, when the probes interchange the roles of being closest and furthest away from the wake. For a higher potential on the satellite in the same plasma conditions, the wake would grow bigger and the potential difference between the two probes would increase even for small angles relative to the positive x -axis. Consequently, the relatively flat region around the inflection point would get steeper and be less evident. Conversely, this region will be more distinguished for a low potential. The plasma density and temperature will also influence the shape of the plot. This can be seen in section 5.3.2, where a second simulation with the same spacecraft geometry, but with $n_0 = 0.10 \text{ cm}^{-3}$ and $T_e = T_i = 1.0 \text{ eV}$ is presented.

Since the shapes of the potential difference curves depend on the spacecraft potential and the plasma parameters, such as the electron temperature and the plasma density, the data from the electric field measurements in the spinning frame might be used to determine these different parameters. It is therefore of great interest to get a better picture of the curves, which can be achieved by examining their frequency contents. We now look at the frequency content of the plot in figure 18(a) by taking the Fourier transform of the data. The result is shown in figure 19, where the amplitudes for each frequency give the corresponding Fourier series coefficient. Since the function in figure 18(a) is odd, there should only be contributions for odd frequencies. This can easily be verified by looking at figure 19. Using the results from the Fourier transformation, we can represent the plot of the difference in potential by the following Fourier series:

$$\Phi_{\text{diff}} = -392 \sin(\theta) + 114 \sin(3\theta) - 16.6 \sin(5\theta), \quad (27)$$

where Φ_{diff} is given in mV.

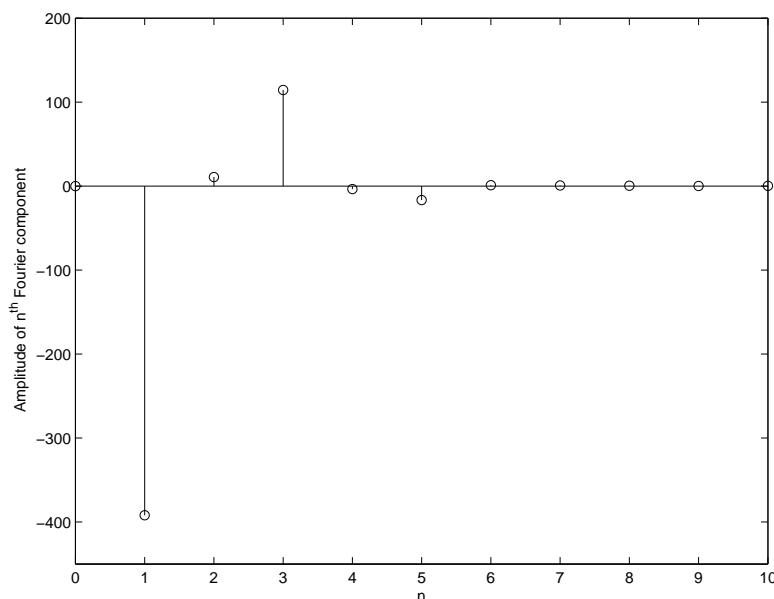


Figure 19: The Fourier transform of the plot in figure 18(a).

The effective potential is as in the previous case calculated by comparison with analytical models. In this case, we look at the potential distribution around a sphere at potential V , which is given by

$$\Phi(r) = V \frac{a}{r}, \quad (28)$$

where a is the radius of the sphere and r the distance from its midpoint. The potential of a sphere with right dimensions is expected to approximate well the cylindrical shaped spacecraft body. We choose to set the surface area of the sphere (A_s) and the cylinder (A_c) equal, since the charge which gives rise to the spacecraft potential, is distributed over the surface:

$$A_s = A_c$$

$$4\pi r_s^2 = 2\pi r_c^2 + 2\pi r_c h$$

$$r_s = \sqrt{\frac{1}{2}r_c(r_c + h)}$$

With the dimensions of the cylinder, $r_c = 1.45$ m and $h = 1.3$ m, we get a radius of the sphere, $r_s \approx 1.4$ m. As before, we try to fit the analytical plot to the simulation data around 10 V and below. Also in this case, an effective potential of 35 V gives a good approximation as can be seen in figure 20. The approximation is better for the spacecraft body than for the booms, which can be understood by the fact that the dimensions of the computational cells are relatively close to the real dimensions of the spacecraft. This is not the case for the boom.

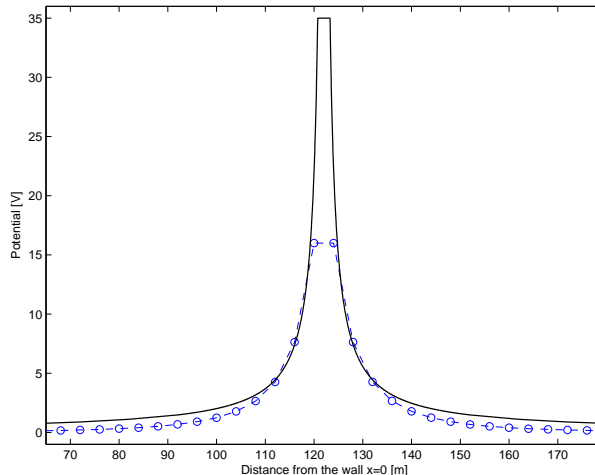


Figure 20: The potential from the simulation with the spacecraft body (dashed blue) plotted together with the analytical potential distribution around a sphere (black). The effective potential is around 35 V.

For both the nominal simulations, the notion of effective potentials has proved to be very useful. A natural question to pose is therefore when the effective potential can be used. One requirement is that few ions should reach regions with higher potential than the simulation potential. In the present case, with flow and thermal energies of 10 eV and 2 eV, respectively, only a fraction $e^{(10-16)/2} = e^{-3} \approx 5\%$ of the ions can be expected to come close to the boom in the simulation, and hence enter regions where the boom potential is inaccurately modelled. The ion density in the wake can therefore be assumed to be correctly estimated. However, we can obviously not go to much lower simulation potentials than this: a simulation potential of 12 V would mean that as many as $1/e \approx 35\%$ of the ions can reach the boom, and the errors in the wake ion density could be expected to be significant in this case. We should also note that while the use of effective potential can be justified for the ion density, the electron density is likely to be too low. In reality, the electrons would be stronger attracted by the real potential than by the lower value of the simulation potential. Conservation of angular momentum will to some extent limit the agglomeration of electrons around the booms, but we may nevertheless suspect that we underestimate the electron density. However, as long as the Debye length is sufficiently larger than the grid spacing, there will be little effect of space charge accumulation on the potential. Even though the electron density may be underestimated when we use the effective potential, we can thus expect the resulting potential picture to still be reasonably accurate.

Another requirement for the use of effective potentials is that there exist simulation data points close to the ion kinetic energy. This will not be the case for too large grid-sizes, which is discussed below.

5.3 Further simulations

To check the validity of the two nominal simulations, which have given enlightening information on the size of the enhanced wake, we have performed some further simulations. These simulations focus on the following three investigations:

- Impact of the Dirichlet boundary conditions for different sizes of the computational box.
- Possible errors due to the unphysical mass ratio.
- Comparison of the simulation results for varied plasma parameters.

For all but one of these new simulations, we use a simulation with booms only as a reference, since the wake is bigger and the boundary conditions ought to have more influence. To be able to perform the simulations in a reasonable time, we switch to a grid with dimensions $8 \times 8 \times 8 \text{ m}^3$. When switching we have to be careful concerning the potential of the boom; as the grid-size increases, the effective potential will also increase. Therefore we will have to reduce the input potential on the discrete grid points constituting the boom. The choice of input potential is complicated by the fact that the method of effective potentials breaks down for a grid-size as large as $8 \times 8 \times 8 \text{ m}^3$. One grid step out from the boom the potential has already decreased to a value much lower than the kinetic energy of the ions (10 eV), which means that we have no data to be fitted to the analytical models. Therefore, we need another approach, to obtain a reference simulation with 8 m-grid with the same effective potential as the simulation in section 5.1. Comparing the potential distribution around the boom for the simulation in section 5.1 with a number of test simulations with different input potentials, we can determine which input potential should be used for the reference simulation with 8 m-grid. The tests showed that an input potential of 16 V for the 8 m-grid is approximately equivalent of 20 V for the 4 m-grid. In the reference simulation, the input potential is thus changed to 16 V and the effective potential is the same as before, 35 V. The minimum value of the potential in the reference simulation is the same as the simulation in section 5.1 (-0.80 V), whereas the difference in potential of 530 mV is somewhat higher. However, this value should be compared to the difference in potential two grid points away from the boom ends for the simulation in section 5.1, since this simulation has a grid of $4 \times 4 \times 4 \text{ m}^3$. At this distance Φ_{diff} reaches its maximum value 520 mV, which is close to the value in the 8 m-grid reference simulation. Besides the potential, we also have to change the number of grid points in each direction, which is halved for the reference simulation. All other parameters remain the same as in the simulation in section 5.1. The output data from the simulations are averaged over the time period $30 \omega_{\text{pe}}^{-1} - 60 \omega_{\text{pe}}^{-1}$, unless otherwise stated.

5.3.1 Numerical variations

The impact of the boundary conditions are investigated by a couple of simulations presented in table 1. The number of grid points in the reference simulation described above is changed for the simulations N1-N4, leaving all other parameters constant. Φ_{min} is the minimum potential in the wake and Φ_{diff} is the difference between the grid points 8 m out from each end of the boom.

In the first test simulation (N1), we have increased the size of the box with a factor of approximately 1.5, while the second simulation (N2) has its dimension decreased by a factor 1.5. When increasing the size of the box, Φ_{min} and Φ_{diff} change only

Simulation	N_x	N_y	N_z	Φ_{\min} [V]	Φ_{diff} [mV]
Reference	30	60	30	-0.80	530
N1	46	90	46	-0.82	540
N2	20	40	20	-0.79	500
N3	16	32	16	-0.72	360
N4	16	32	8	-0.56	280

Table 1: Impact of boundary conditions.

moderately, which means that the reference simulation is close to the limit where the Dirichlet conditions do not influence the final result. For test simulation N2, the changes are still small, but examining the potential plots, we can see that the contours look somewhat "squeezed" into the computational box. This phenomenon gets more and more pronounced, the smaller the computational box, which can be seen in figure 21, showing the potential in the xy-plane from the third test simulation (N3). In this simulation, the differences in Φ_{\min} and Φ_{diff} get significant. The boom tips are only 4 grid points ($= 32 \text{ m} \sim 1\lambda_D$) away from the wall, explaining the large decrease in Φ_{diff} . In the last simulation (N4), we set also the vertical distance (in the z -direction) between boom and walls equal to 4 grid points, which has a larger influence on the size of the wake than the other limitations of the size of the computational box. This can be understood by the fact that most of the ions flowing towards the boom will be deflected in the vertical direction, a phenomenon clearly visible in figure 11(b) for the nominal simulation with booms.

The main conclusion from this set of simulations is that the boundary conditions have a large impact on the final results, yet not as large as to invalidate our results. The second simulation shows that we could have chosen a computational box with dimensions $160 \times 320 \times 160 \text{ m}^3$ even for the nominal simulations in sections 5.1 and 5.2. As has been mentioned, the potential structure close to the borders will be affected by the Dirichlet conditions, which is also true for the electron density. The ion density, on the other hand, is relatively unaffected by small potential differences and thus also by the boundary conditions, why the ion wake will be able to extend out through the boundaries keeping the same overall shape. This explains why the influence of the boundaries are moderate.

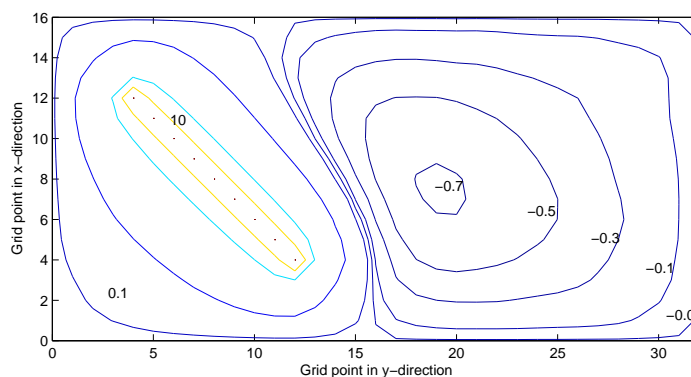


Figure 21: The potential in the xy-plane from simulation 3 in table 1. The grid spacing is 8 m.

As for the mass ratio, we have run one simulation with the physical mass ratio between protons and electrons of $m_p/m_e = 1836$. (Only protons are modelled, neglecting the second most important ions in the polar wind, the oxygen ions, O^+ , with a mass

ratio of about 30000.) The rest of the parameters are the same as in the reference simulation in table 1 with one exception; while the energy of the protons will remain the same as before, the velocity will decrease. The steady state of the simulation will thus be established later, leading to longer convergence times. For this simulation, we average the output data over the time period $100 \omega_{pe}^{-1} - 250 \omega_{pe}^{-1}$. The minimum value in the wake is -0.92 V, which is 15% lower compared with the reference simulation. Surprisingly, $\Phi_{diff}=350$ mV, which is much lower than in the reference simulation. This means that for a physical mass ratio we get a deeper, but less wide wake. The lower value for Φ_{diff} in this simulation indicates that we have made an overestimation of the spurious electric field in the previous simulations.

5.3.2 Variation of plasma parameters

Booms only In this section we will investigate the effects of variation of the physical parameters for two different simulations. We use the same reference simulation as in the previous case. For both of the simulations, we keep the Debye length constant at the same value as before (around 24 m). To achieve this we vary the temperature and the plasma density in equal proportions, since the Debye length is proportional to $\sqrt{\frac{T_0}{n_0}}$. The relevant parameters for these simulations are shown in table 2.

Simulation	T_e [eV]	n_0 [cm^{-3}]	u_i/v_{th}^i	u_i/v_{th}^e	V_s^{in} [V]	V_s^{eff} [V]
Reference	2.0	0.20	3.2	0.32	16	35
P1	1.0	0.10	4.5	0.45	20	45
P2	4.0	0.40	2.2	0.22	14	31

Table 2: Parameters for simulations, where the physical parameters are varied.

The ratio between the flow velocity and the thermal velocity of the ions, is called the ion *Mach number*. Large Mach numbers will cause a large ion wake, while smaller Mach numbers cause smaller wakes. The effective potential can not be calculated as in sections 5.1 and 5.2, because of the large grid-size. Instead, we have to use a simpler and less adequate method. The reference simulation gets an effective potential of 35 V by comparison with the simulation in section 5.1 (see above). For simulations P1 and P2, the input potential should be chosen in such a way that the effective potential follows the density-potential relation given by Pedersen [19]. A density of 0.1 cm^{-3} corresponds to a potential of around 45 V, while 0.2 cm^{-3} corresponds to approximately 25 V. To estimate the input potentials, we assume that the effective potential depends linearly on the input potential. For simulation P1, this gives an input potential of $16/35 \times 45 \approx 20$ V. To model an effective potential of 25 V for simulation P2, we would need an input potential of $16/35 \times 25 \approx 11$ V. However, the choice of 11 V is not possible, since the total energy of the ions equals $E_{\text{tot}} = E_k^i + KT_i = 14$ eV, which means that all ions would be able to reach the boom. Even for an input potential of 14 V, which is chosen in simulation 2, many ions can reach the boom. Therefore the results from simulation P2 should be interpreted with care. The value of 14 V is taken as a compromise between a potential satisfying $eV_s > E_{\text{tot}}$ and a potential obeying the density-potential relation. Results from simulations P1 and P2, i. e. Φ_{min} and Φ_{diff} , are shown in table 3.

Due to the large Mach number, the ion wake for simulation P1 will be larger than the wakes in both the reference simulation and simulation P2. Nevertheless, the potential structure of the wake is less deep, since the plasma density is low, which means that less electrons fill the wake. Moreover, their thermal velocity is lower, so that the small

Simulation	Φ_{\min} [V]	Φ_{diff} [mV]
Reference	-0.80	530
P1	-0.70	410
P2	-0.77	630

Table 3: Results from the simulations, described in table 2.

potentials in the wake prevent the electrons from entering more effectively. Conversely, in simulation P2, the ion wake is small, but it is filled with many electrons, creating a deeper wake than in simulation P1. Even if $|\Phi_{\min}|$ is smaller in simulation P2 than in the reference simulation, the difference in potential between the boom ends gets bigger. One possible explanation for this is based on the larger mobility of the electrons; they will not equalize the potential difference at the boom ends to the same extent, since they are less governed by the potential structures.

Spacecraft body without booms In this simulation we are interested in the influence of variations in the plasma density and temperature for a spacecraft without booms. We use the same grid as in section 5.2, since the size of the spacecraft would be too big for an 8 m-grid. As in simulation P1, the Debye length is held constant, reducing the plasma density and the temperature by equal amounts: $n_0 = 0.1 \text{ cm}^{-3}$ and $T_e = T_i = 1.0 \text{ eV}$. This means that the effective potential again should be around 45 V, which is obtained for an input potential of 20 V. In figure 22 the angular dependence of the potential difference from this simulation (blue) is plotted together with the corresponding plot for the simulation in section 5.2 (black). As can be seen, the maximum difference is lower than in the previous simulation and the region around the inflection point is more enhanced. This is explained by the fact that the wake does not grow bigger, despite the higher potential, since there are less electrons to fill the wake. The minimum potential in the wake is -0.32, which should be compared with the minimum of -0.34 of the simulation in section 5.2. Moreover, the potential from the spacecraft will decrease more slowly, creating a less wide wake, which will give lower potential differences.

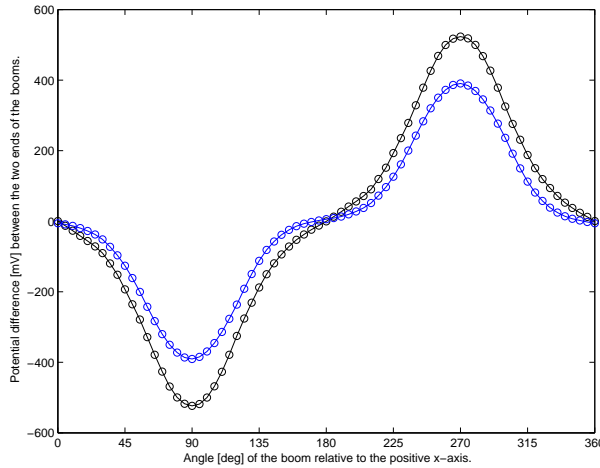


Figure 22: Potential difference between the probes at different angles of the boom relative to the flow for two cases: **1.** $V_s^{\text{in}} = 16 \text{ V}$, $V_s^{\text{eff}} = 35 \text{ V}$, $n_0 = 0.2 \text{ cm}^{-3}$, $T_e = T_i = 2.0 \text{ eV}$ (**black**, see figure 18(a)). **2.** $V_s^{\text{in}} = 20 \text{ V}$, $V_s^{\text{eff}} = 45 \text{ V}$, $n_0 = 0.1 \text{ cm}^{-3}$, $T_e = T_i = 1.0 \text{ eV}$ (**blue**).

6 Discussion

The PIC method implemented in PicUp3D has shown to accurately model the phenomenon of enhanced wakes in cold tenuous plasmas. Nevertheless, a better resolution in the numerical computations would certainly be desirable: a finer grid with more computational cells would provide more details and more macro-particles per computational cell would reduce the numerical noise. For reasonable convergence times (less than a week), this is, however, not possible when running the simulations on ordinary PCs, if we do not change the physical parameters. In the two simulations in sections 5.1 and 5.2, for example, more than 4 million particles have to be moved in each time step. These simulations have taken about five days to converge. Increasing the number of computational cells or macro-particles would generate even longer simulation times. The use of an adaptive-grid would solve this problem, making the grid finer at the vicinity of the spacecraft and larger further away. The number of computational cells could thus be reduced and still yield a better resolution. With fewer computational cells, we do not need as many macro-particles for the same level of numerical noise.

An adaptive-grid would also model the potential distribution close to the thin booms more correctly. As has been seen, the large grid-sizes of 4 m and 8 m result in too high values for the grid points closest to the boom. We have been able to circumvent this problem for the 4 m-grid by introducing the notion of effective potentials, where we compare the data close to the boom with analytical models. The validity of this method should clearly be verified by use of an adaptive-grid code. The use of effective potentials showed very useful for the presented simulations with 4 m-grid, but it has two major drawbacks:

1. To be able to fit the analytical models to the simulation data, we need potential data points close to the values of the ion kinetic energy. For the 8 m-grid, the potential has already decreased to too low values at the first data point.
2. The input potential of the spacecraft has to exceed the total energy of the ions, otherwise the ions can reach the spacecraft. This makes it difficult to model warmer, denser plasmas, in which the measured spacecraft potentials are low.

Another closely related advantage of adaptive-grid codes is that we would be able to model the spacecraft structure in more details, including for example the effect of the guards of the booms.

The impact of the Dirichlet boundary conditions on the potential is not as important as we expected at first, and it is even possible to reduce the size of the computational box for the two nominal simulations in sections 5.1 and 5.2. Nevertheless, for flowing plasma simulations, it would be better to implement Neumann conditions ($\frac{\partial \Phi_p}{\partial r} = 0$) on all boundaries, except on the boundary of the inflow, where the potential should be fixed. This would reduce the effect of the boundary conditions on the potential structure, allowing a choice of an even smaller computational box.

Our simulations are of course only an approximation of the physical reality for the Cluster satellites in the polar wind. We have for example neglected the emission of photoelectrons and the magnetic field. The emission and exchange of photoelectrons by different electrical elements on the spacecraft might be important. The wake could for example to a large extent be filled with photoelectrons emitted from the probes and their bootstrapped elements rather than with natural plasma electrons. In the current release of PicUp, it is possible to model photoemission from the spacecraft body itself, whereas the emission from the booms is neglected, which is compensated by also

neglecting the recollection of electrons on the booms. Further simulations including photoelectrons are therefore indeed realizable. The magnetic field could be important only for the electrons, since their Larmor radius is close to the scale of the problem. Neglecting the magnetization of the electrons could lead to an underestimation of the negative potential of the wake. The mass ratio between electrons and ions in the simulations is much lower than the physical mass ratio, as this will give shorter convergence times. A test with the real mass ratio between electrons and protons have shown that we have overestimated the spurious electric field caused by the wake. However, the simulation with real mass ratio still gives results which are close to the results from the reference simulation, since the energy of the particles is conserved along their trajectories. Finally, the models of the spacecraft are extremely simplified, either modelling only the spacecraft body itself or the booms. For detailed descriptions of the spacecraft adaptive-grid codes are necessary, as has been discussed above, but even for the 4 m-grid we could get a more correct picture by combining the simulation of the spacecraft body with the simulation of the booms. The results from such a simulation would probably look very much like the results from the boom simulation, since the booms have turned out to be the most important structure for wake formation.

7 Conclusions

When operating in the polar wind, the Cluster satellites experience problems for the electric field instrument EFW. Comparing data from EFW with data from the other electric field instrument on Cluster, EDI, an electric field of non-geophysical origin in the direction of the flowing polar wind can be seen in the EFW data. To get maximal scientific return from the instruments, it is necessary to understand how such spurious electric fields arise. Eriksson et al. [1] suggested that the spurious electric field was caused by an enhanced wake behind the spacecraft. The plasma in the polar wind is both cold and tenuous, which ensures that $KT_i < \frac{m_i u^2}{2} < eV_s$. As the kinetic energy of the ions is higher than their thermal energy, wakes may form behind any obstacle. At the same time, the spacecraft is charged to sufficiently high positive potentials that the ions will not have enough energy to reach the spacecraft. Therefore, the size of the wake will be determined by the potential distribution around the spacecraft, increasing the wake considerably.

Simulations of spacecraft-plasma interactions in polar wind conditions have been performed with the simulation code package PicUp3D, which has verified the model for the errors in the measurements for EFW. The simulations have also given a quantitative picture of the wake structure and we have been able to estimate the impact on the electric field instrument. Two different types of simulations have been carried out; one modelling the spacecraft booms only, and the other the spacecraft body itself without booms. Comparison between these simulations shows that the booms have the largest impact on wake formation. Assuming the probes of EFW perfectly couple to the plasma, we have derived the non-geophysical field, caused by the wake of a boom at 45° to the flowing plasma, which resulted in around 5 mV/m. This is consistent with data from the EFW measurements. For the simulation with the spacecraft body, we were able to find an angular dependence of the spurious electric field, which provided explanation for repeated flat regions found in spin fitted electric field data. The maximum potential difference was around 7 mV/m for booms aligned with the flow. We have also studied the effect of variation of the plasma parameters.

Apart from providing interesting physical results, this project has shown that PicUp3D is possible to use for simulation of wake problems. The possibility of running the code on common PCs, as well as the open source philosophy, has been of great advantage for scientific use. In this study, the main problem of PicUp3D has been the inability of modelling thin booms, which leads to an underestimation of the boom potential. However, we have been able to avoid this problem by introducing an effective boom potential. The validity of this method should be investigated using adaptive-grid codes. Such codes would also be useful for a more detailed description of the spacecraft structures. Another concern during the work with the simulations has been the impact of the Dirichlet boundary conditions. Several tests have shown that the boundary conditions do not influence the overall structure of the wake in the nominal simulations (see sections 5.1 and 5.2). These tests also show that we could reduce the size of the computational boxes for the two nominal simulations by a factor as big as 1.5, without considerably affecting our final results. Nevertheless, for this kind of problem, Neumann conditions on all sides except the inflowing boundary are better suited.

In future simulations the effect of emission of photoelectrons and magnetized plasma electrons should be investigated. It would also be rewarding to model a more realistic spacecraft geometry with both body and booms, including the guard, which probably will affect the details of the potential around the probes. An extension of this type of simulations should moreover concentrate on deriving scaling parameters: re-

sults describing the quantitative dependence of the wake structure on different input parameters, such as spacecraft potential, flow speed and electron temperature, would be of great interest.

8 Acknowledgements

This project was initiated by Mats André and Anders Eriksson at the *Swedish Institute of Space Physics, Uppsala Division (IRF-U)*. They are sincerely thanked for defining and supporting the project. As my supervisor for this project, Anders Eriksson has moreover provided invaluable help, encouragement when needed, and above all a lot of enthusiasm. Alain Hilgers and Benoit Thiébaud at ESTEC¹⁶ are thanked for their hospitality and important help in the initial phase of the project. I would also like to thank Lars Daldorff (Department of Astronomy and Space Physics, Uppsala University) for many clarifying discussions on PIC code simulations, and Julien Forest (Swedish Institute of Space Physics, Kiruna Division) for help with trouble-shooting. Finally, Tobias Eriksson and Yuri Khotyaintsev (IRF-U) are recognized for their support of the simulation computers.

¹⁶European Space Research and Technology Center, Noordwijk, Holland

References

- [1] A. Eriksson, M. André, B. Klecker, H. Laakso, P.-A. Lindqvist, F. Mozer, G. Paschmann, A. Pedersen, J. Quinn, R. Torbert, K. Torkar, and H. Vaith. Cluster comparison of the double-probe and electron drift techniques for measuring the electric field. Manuscript in preparation, 2004.
- [2] M. G. Kivelson and C. T. Russel. *Introduction to Space Physics*. Cambridge University Press, Cambridge, 1995.
- [3] G. K. Parks. *Physics of Space Plasmas*. Addison Wesley, Redwood City, 2nd edition, 1991.
- [4] T. I. Gombosi. *Physics of the Space Environment*. Cambridge University Press, Cambridge, 1998.
- [5] I. Sandahl. *Norrskén - Budbärare från rymden*. Atlantis, Stockholm, 1998.
- [6] Y.-J. Su, J.L. Horwitz, T.E. Moore, B.L. Giles, M.O. Chandler, P.D. Craven, M. Hirahara, and C.J. Pollock. Polar wind survey with the Thermal Ion Dynamics Experiment/Plasma Source Instrument suite aboard POLAR. *Journal of Geophysical Research*, 103:29305–29337, 1998.
- [7] F. F. Chen. *Introduction to Plasma Physics and Controlled Fusion*. Plenum Press, New York, 2nd edition, 1984.
- [8] A. I. Eriksson, L. Wedin, J.-E. Wahlund, and B. Holback. Analysis of Freja charging events: Modelling of Freja observations by spacecraft charging codes. IRF Scientific report 252, Swedish Institute of Space Physics, 1999.
- [9] H. B. Garrett. The charging of spacecraft surfaces. *Reviews of Geophysics and Space Physics*, 19(4):577–616, 1981.
- [10] K. Torkar et al. An experiment to study and control the Langmuir sheath around INTERBALL-2. *Annales Geophysicae*, 16:1086–1096, 1998.
- [11] K. Torkar et al. Active spacecraft potential control for Cluster - implementation and first results. *Annales Geophysicae*, 19:1289–1302, 2001.
- [12] C. P. Escoubet, M. Fehringer, and M. Goldstein. The Cluster mission. *Annales Geophysicae*, 19:1197–1200, 2001.
- [13] G. Gustafsson et al. The Electric Field and Wave experiment for the Cluster mission. *Space Science Reviews*, 79:137–156, 1997.
- [14] G. Gustafsson et al. First results of electric field and density observations by Cluster EFW based on initial months of operation. *Annales Geophysicae*, 19:1219–1240, 2001.
- [15] G. Paschmann et al. The electron drift technique for measuring electric and magnetic fields. measurement techniques in space plasmas: Fields. *AGU Geophysical Monograph*, 103, 1998.
- [16] G. Paschmann et al. The Electron Drift Instrument on Cluster: overview of first results. *Annales Geophysicae*, 19:1273–1288, 2001.

- [17] A. Pedersen et al. Electric field measurements in a tenuous plasma with spherical double probes. In *Measurement Techniques in Space Plasmas: Fields*, Geophysical Monograph 103, pages 1–12. American Geophysical Union, 1998.
- [18] E. Engwall, A. Eriksson, A. Pedersen, J. Forest, G. Paschmann, J. Quinn, R. Torbert, and K. Torkar. Wake effects on positively charged spacecraft in flowing tenuous plasmas: Cluster observations and modeling. In *Proceedings of the 8th Spacecraft Charging Technology Conference*. NASA, 2003.
- [19] A. Pedersen et al. Four-point high time resolution information on electron densities by the electric field experiments (EFW) on Cluster. *Annales Geophysicae*, 19:1483–1489, 2001.
- [20] A. Pedersen. Solar wind and magnetosphere plasma diagnostics by spacecraft electrostatic potential measurements. *Annales Geophysicae*, 13:118–121, 1995.
- [21] J. Forest, L. Eliasson, and A. Hilgers. A new spacecraft plasma simulation software, PicUp3D/SPIS. In *7th Spacecraft Charging Technology Conference*, volume SP-476, pages 515–520. ESA, 2001.
- [22] J.-F. Roussel. Spacecraft plasma environment and contamination simulation code: Description and first tests. *Journal of Spacecraft and Rockets*, 35(2):205–211, 1998.
- [23] C. K. Birdsall and A. B. Langdon. *Plasma Physics via Computer Simulations*. Adam Hilger, Bristol, 1991.
- [24] <http://www.univ-orleans.fr/SCIENCES/MAPMO/membres/filbet/vadorh/node2.html>. 2001.
- [25] W. H. Press, S. A. Teukolsky, W. T. Vetterling, and B. P. Flannery. *Numerical Recipes in C*. Cambridge University Press, Cambridge, 2nd edition, 1992.
- [26] N. Singh, B. I. Vashi, and L. C. Leung. Three-dimensional numerical simulation of current collection by a probe in a magnetized plasma. *Geophysical Research Letters*, 21(9):833–836, 1994.
- [27] E. Hallén. Lösung zweier Potentialprobleme der Elektrostatik. *Arkiv för matematik, astronomi och fysik*, 21A, 22, 1929.
- [28] E. Hallén. *Electromagnetic Theory*. Chapman & Hall, London, 1962. Translated from the Swedish edition by R. Gåsström.